The EMBO Journal (2006) 25, 2315–2325 | © 2006 European Molecular Biology Organization | All Rights Reserved 0261-4189/06
www.embojournal.org

THE EMBO JOURNAL

Crystal structure of CHP2 complexed with NHE1-cytosolic region and an implication for pH regulation

Youssef Ben Ammar[1,4], Soichi Takeda[2,3,4], Takashi Hisamitsu[1], Hidezo Mori[2] and Shigeo Wakabayashi[1,*]

[1]Department of Molecular Physiology, National Cardiovascular Center Research Institute, Suita, Osaka, Japan, [2]Department of Cardiac Physiology, National Cardiovascular Center Research Institute, Suita, Osaka, Japan and [3]Laboratory of Structural Biochemistry, RIKEN Harima Institute at SPring-8, Kouto, Mikazuki-cho, Sayo, Hyogo, Japan

The plasma membrane Na^+/H^+ exchangers (NHE) require calcineurin B homologous protein (CHP) as an obligatory binding partner for ion transport. Here, we report the first crystal structure of CHP (CHP2 isoform) in complex with its binding domain in NHE1. We show that the cytoplasmic α-helix of NHE1 is inserted into the hydrophobic cleft formed by N- and C-lobes of CHP2 and that the size and shape of this crevice together with hydrogen bond formation at multiple positions assure a high degree of specificity for interaction with NHE members. Structure-based mutagenesis revealed the importance of hydrophobic interactions between CHP/NHE1 for the function of NHE1. Furthermore, the crystal structure shows the existence of a protruding CHP-unique region, and deletion of this region in CHP2 inhibited the NHE1 activity by inducing the acidic shift of intracellular pH dependence, while preserving interaction with NHE1. These findings suggest that CHP serves as an obligatory subunit that is required both for supporting the basic activity and regulating the pH-sensing of NHE1 via interactions between distinct parts of these proteins.

The EMBO Journal (2006) **25**, 2315–2325. doi:10.1038/sj.emboj.7601145; Published online 18 May 2006
Subject Categories: membranes & transport; structural biology
Keywords: calcineurin homologous protein; crystal structure; Na^+/H^+ exchanger; pH regulation

Introduction

Maintenance of intracellular pH (pH_i), Na^+ concentration, and cell volume is crucial for all living cells to survive and to ensure a variety of cellular functions, such as cell metabolic processes, muscle contraction, secretion, and higher-order brain activity. The Na^+/H^+ exchanger (NHE) is an important transporter regulating such ionic homeostasis and catalyzing the electroneutral countertransport of Na^+ and H^+ through the plasma membrane and other intracellular organellar membranes in various animal species (Wakabayashi *et al*, 1997; Counillon and Pouyssegur, 2000; Putney *et al*, 2002; Orlowski and Grinstein, 2004; Zachos *et al*, 2005). Of the nine different NHE isoforms identified to date (NHE1–NHE9), the ubiquitous isoform NHE1 has been studied most extensively. NHE1 is known to be activated rapidly in response to various extracellular stimuli, such as hormones, growth factors, and mechanical stressors (Wakabayashi *et al*, 1997; Orlowski and Grinstein, 2004). Such activation of NHE1 is often linked to various diseases. For example, elevated NHE1 activity is thought to be a risk factor causing heart failure and hypertrophy, as evidenced by the remarkable protective effects of specific inhibitors (Karmazyn, 2001; Engelhardt *et al*, 2002). Regulation of NHE1 is thought to occur through interaction of multiple signaling molecules with the carboxyl (C)-terminal cytoplasmic domain of NHE1 and subsequent conformational change of the amino (N)-terminal transmembrane domain responsible for catalyzing NHE (see Figure 1A for membrane topology). Importantly, this regulation of NHE1 is attributable to a change in the affinity for intracellular H^+. A previous biochemical experiment using membrane vesicles suggested that the exchangers possess a cytoplasmic 'H^+-modifier' or 'pH-sensor' site(s), distinct from the H^+-transport site (Aronson *et al*, 1982; Wakabayashi *et al*, 2003a). The exchangers were thus considered to be activated through conformational changes caused by protonation of this regulatory site. Our recent study, using cells expressing NHE isoforms (NHE1–3), further supported this concept by measuring the reverse reaction of exchange (Na^+ efflux) (Wakabayashi *et al*, 2003a). However, another recent study reported an allosteric model with no additional H^+-modifier site to explain the sigmoidal cytosolic H^+ dependence (Lacroix *et al*, 2004).

Of the signaling molecules that interact with the exchanger, calcineurin B (CNB) homologous protein (CHP) is particularly important. CHP was initially identified as a protein (p22) involved in vesicular transport (Barroso *et al*, 1996) and that interacts with NHE (Lin and Barber, 1996). CHP is a Ca^{2+}-binding protein with EF-hand motifs and is myristoylated at the N-terminus (Gly2) (Barroso *et al*, 1996; Lin and Barber, 1996). To date, three CHP isoforms with different tissue expression patterns have been identified in mammalian tissues. While CHP1 is expressed ubiquitously in virtually all tissues, the expression of CHP2 is restricted to cancer cells (Pang *et al*, 2002) and the small intestine (Inoue *et al*, 2003), and that of CHP3 (also called tescalcin) is restricted to the heart, brain, stomach, and testis (Mailander *et al*, 2001; Perera *et al*, 2001; Gutierrez-Ford *et al*, 2003). Previously, we reported that CHP (at least CHP1 and CHP2) is an essential cofactor supporting the physiological activity of the plasmalemmal NHE by interacting with the juxtamembrane cyto-

*Corresponding author. Department of Molecular Physiology, National Cardiovascular Center Research Institute, Fujishirodai 5-7-1, Suita, Osaka 565-8565, Japan. Tel.: +81 6 6833 5012; Fax: +81 6 6835 5314; E-mail: wak@ri.ncvc.go.jp
[4]These authors contributed equally to this work

Received: 5 December 2005; accepted: 24 April 2006; published online: 18 May 2006

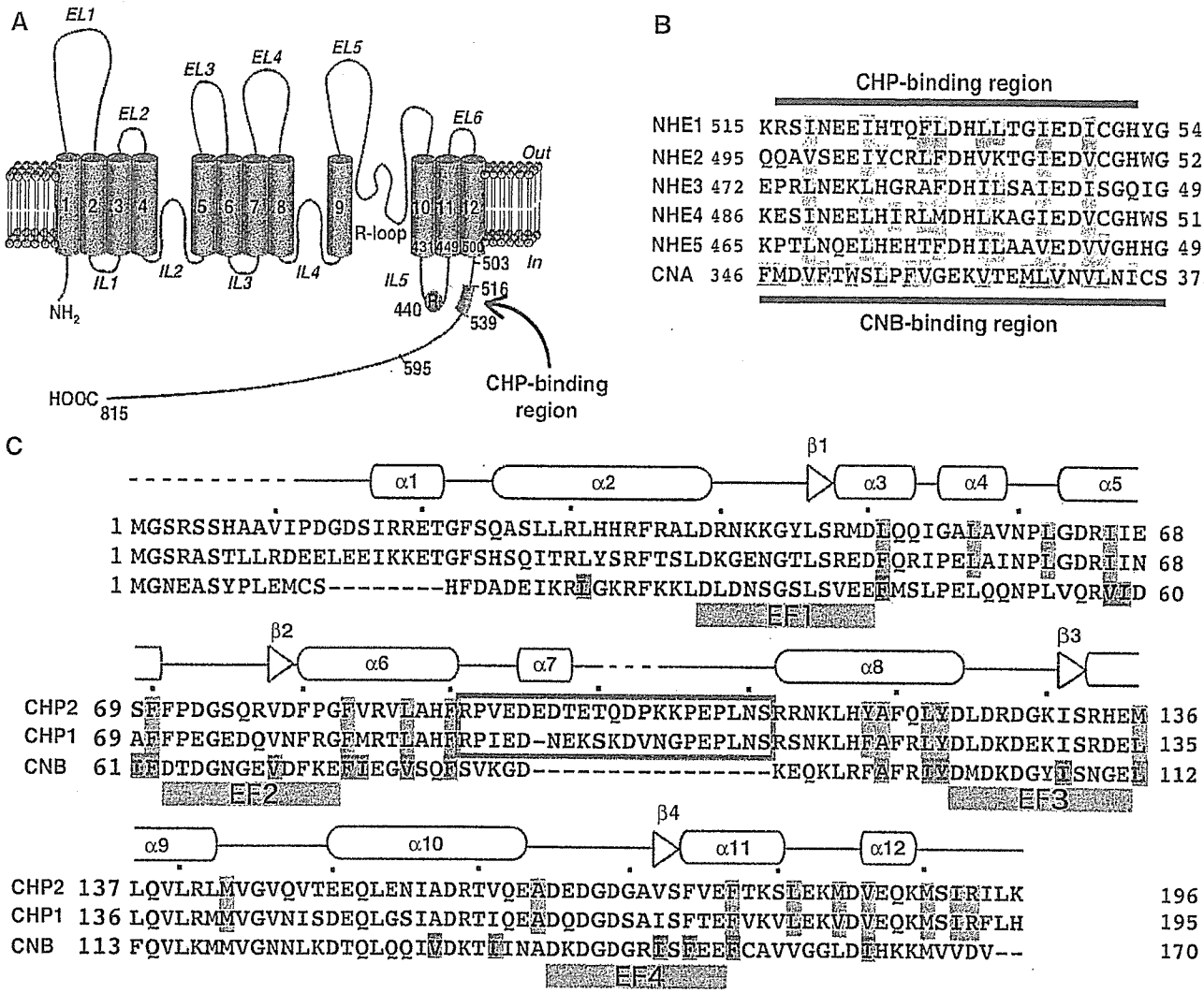

Figure 1 Sequence alignments of CHP and its binding domain in NHE isoforms. (**A**) Membrane topology model of NHE1. NHE1 consists of the N-terminal transporter domain with 12 transmembrane domains (TM) and a long C-terminal regulatory domain. Six extracellular (EL) and five intracellular loops (IL) are mapped. CHP binds to the juxtamembrane cytoplasmic domain. Arg440 was identified as an important residue for NHE1 regulation. (**B**) Amino-acid sequences for human NHE1–NHE5 (Genbank Accession Numbers: NM_003047, NM_003048, NM_004174, NM_177084, and NM_004594, respectively) are aligned together with sequence of CNB-binding region in CNA (Q08209). Hydrophobic residues involved in interaction with CHP or CNB are highlighted in green. Residues in NHE1 forming hydrogen bonds with CHP2 are shown in *red*. (**C**) Amino-acid sequences of CHP1/2 and CNB (Q99653, Q9D869, and P63098). Secondary structural elements are based on the structure of CHP2/NHE1-peptide complex. Loops of four EF-hands are shown by *green* boxes, but EF1 and EF2 are ancestral sites that do not coordinate Ca^{2+}. Hydrophobic residues involved in interaction with NHE1 or CNA are highlighted in *blue* and *red*, respectively. Central CHP-unique region is *boxed*. Residues in CHP2 forming hydrogen bonds with NHE1 are shown in *red*.

plasmic domain of NHE1 to NHE3 (Pang *et al*, 2001, 2002). CHP binding-defective mutant exchangers (NHE1-3) exhibited low exchange activity (Pang *et al*, 2001) (5–10% of the wild-type level) and greatly shifted the pH_i-dependence to the acidic side (Pang *et al*, 2004), suggesting that the juxtamembrane region with bound CHP would therefore function as a key structure maintaining the physiologically active conformation of NHE1. Recently, the crystal structure of CHP1 was solved as a single polypeptide without the target molecule (Naoe *et al*, 2005). However, this structure did not provide information about the interaction(s) with NHE.

To obtain insights into the molecular mechanisms of the interaction(s) with NHE and regulation of NHE by CHP, we determined the crystal structure of CHP (CHP2 isoform) complexed with its binding region in NHE1. Herein, we report that the α-helical CHP-binding region of NHE1 is inserted into the hydrophobic cleft formed by residues in the N- and C-lobes of CHP2 through strong hydrophobic interactions as well as hydrogen bond formation. Structure-based mutational analysis revealed that CHP may activate the exchanger by associating its hydrophobic cleft and also regulate the pH-sensing of NHE1 via its central CHP-unique region connecting the two lobes of CHP.

Results

Overall structure of CHP2 in complex with the cytoplasmic binding region of NHE1

We crystallized the His_6-tagged human CHP2 (1–196) complexed with its binding domain (aa 503–545) in NHE1 (referred to as CHP2/NHE1-peptide) in the presence of yttrium, initially solved the structure by MAD phasing, and refined the structure model to 2.7 Å (Table I). Figure 2 shows

Table I Data collection, phasing and refinement statistics

	High resolution data	MAD		
Data collection				
Space group	$P4_3$		$P4_3$	
Cell dimensions				
a, *b*, *c* (Å)	49.96, 49.96, 103.2		49.96, 49.96, 103.2	
α, β, γ (deg)	90, 90, 90		90, 90, 90	
		Peak	*Inflection*	*Remote*
Wavelength	1.0000	0.7270	0.7266	1.0000
Resolution (Å)	50–2.7	50–3.0 (3.11–3.00)	50–3.0 (3.11–3.00)	50–3.0 (3.11–3.00)
R_{merge}[a]	4.8 (25.1)	0.084 (0.311)	0.073 (0.297)	0.072 (0.330)
$I/\sigma I$[b]	17.3 (4.5)	14.9 (4.1)	15.9 (5.0)	15.8 (3.6)
Completeness (%)[b]	97.3 (83.1)	98.5 (87.5)	98.5(87.5)	97.8 (80.9)
Redundancy[b]	4.0 (3.1)	7.2 (5.6)	7.3 (5.7)	7.1 (5.3)
Refinement				
Resolution (Å)	50–2.7			
No. reflections	6746			
R_{work}/R_{free}	0.218/0.287			
No. atoms				
Protein	1674			
Ligand/ion	2			
B-factors				
Protein	72.5			
Ligand/ion	70.5			
R.m.s. deviations				
Bond lengths (Å)	0.005			
Bond angles (deg)	1.00			
Ramachandran plot (%)				
Favorable	87.2			
Allowed	12.8			
Generously allowed	0			
Disallowed	0			

[a]$R_{merge} = \sum_{hkl} \sum_i |I_i(hkl) - \langle I(hkl) \rangle| / \sum_{hkl} \sum_i I_i(hkl)$, where $I_i(hkl)$ is the *i*th intensity measurement of reflection *hkl*, and $\langle I(hkl) \rangle$ is its average.
[b]Highest resolution shell is shown in parentheses.

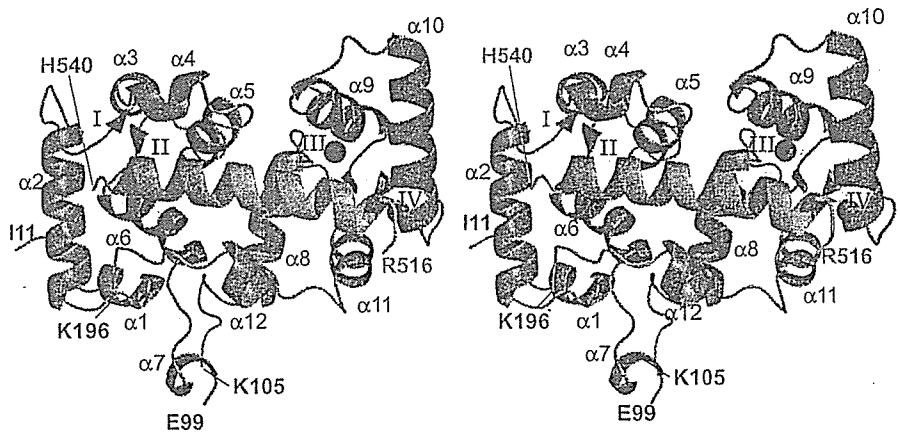

Figure 2 Stereo view of the CHP2/NHE1-peptide complex showing the overall structure. N- and C-lobes of CHP2 are colored *red* and *blue*, respectively. The NHE1 peptide is colored *green*. *Pink* spheres represent the two yttrium ions coordinated by EF3 and EF4.

the overall structure of the complex CHP2/NHE1-peptide. The structural model contains 181 amino acids from CHP2 (Ile11–Glu99 and Lys105–Lys196), and 25 amino acids from NHE1 fragment (Arg516–His540). The polypeptide chain of CHP2 with dimensions of $55 \times 47 \times 28$ Å is folded into two globular domains (N- and C-terminal lobes) composed of 12 α-helices (α1–α12) and four short β-strands (β1–β4). Two Y^{3+} ions were found to associate with EF3 and EF4 in the C-lobe (Figure 2), consistent with biochemical data showing the high-affinity binding of Y^{3+} (~1 nM) to CHP2 (Supplementary Figure 1). The overall structure of CHP2 is close to the Ca^{2+}-bound form of NHE-free CHP1, which was solved recently (Naoe *et al*, 2005; Supplementary Figure 2). Indeed, the distances between metal ions and coordinating oxygen atoms are almost the same for Y^{3+} in CHP2 (2.38 ± 0.2 Å) and Ca^{2+} in CHP1 (2.40 ± 0.1 Å). In addition, the

Y^{3+}-bound form of CHP2 preserved the ability to interact with the full-length NHE1 (Supplementary Figure 1). Therefore, we consider our solved structure compatible with the Ca^{2+}-bound form of CHP2. The overall structure of CHP2 is also similar in folding topology to the structures of other EF-hand-containing proteins, including CNB (Kissinger *et al*, 1995), K^+-channel interacting protein (KChIP1) (Zhou *et al*, 2004; Supplementary Figure 2), AtCBL2 (Nagae *et al*, 2003), NCS-1 (Bourne *et al*, 2001), neurocalcin (Vijay-Kumar and Kumar, 1999), and CIB (Gentry *et al*, 2005). A common structural feature of these proteins is that they all have four EF-hands in pairs such that EF1 and EF2 form the N-lobe and EF3 and EF4 form the C-lobe. However, some local differences were observed between CHP2 and CNB or between CHP2 and KChIP1. For example, the orientation of EF-hand α-helices is different among these molecules because of the swiveling motion between the N- and C-lobes of each molecule, although each pair of EF hands is relatively fixed via hydrogen bonds. This may explain the incomplete superposition between overall structures of CHP2 and CNB (root mean square deviation, r.m.s.d. 1.7 Å), in contrast to the relatively good superposition between the N-lobes or between the C-lobes themselves (r.m.s.d. 1.3 or 1.0 Å, respectively). Although CHP2 and CNB have about 36% identity in their amino-acid sequences (Figure 1C), CHP2 coordinates two Ca^{2+} ions in EF3 and EF4, unlike CNB capable of coordinating four Ca^{2+} ions in its four EF-hands (Kissinger *et al*, 1995). Lack of Ca^{2+}-coordination in EF1 and EF2 would be derived from significant deviation from the canonical EF-hand sequence and resulting atypical structure, as described previously in detail (Naoe *et al*, 2005).

The most remarkable difference between CHP2 and other calcium binding proteins is that the N- and C-lobes of CHP2 are linked by a long flexible region, which protrudes by a length of about 14 Å for the determined region (Figure 3A). This domain, referred to as the CHP-unique region, was not found in other Ca^{2+}-binding proteins. Five residues, Thr100 to Lys104, were not assigned in the structure due to the absence of their electron density map. Particularly, the region from aa 93–108 did not make any contact with other regions of CHP2. In addition, we found that the side chain oxygen atoms of Asp95 in this region coordinate Y^{3+} in the neighboring molecule in the crystal and thus participate in stabilization of this region. This observation explains why CHP2/NHE1-peptide was crystallized only in the presence of Y^{3+}. These findings suggest that the CHP-unique region is very flexible in aqueous solution. This is consistent with the finding that this region was not seen in the structure of NHE-free CHP1 (Naoe *et al*, 2005), which was solved in different crystal packing.

Interaction between CHP2 and its binding domain in NHE1

Structure determination of the complex revealed the orientation of CHP2 toward the cytoplasmic region of NHE1. The N- and C-terminal halves of the cytoplasmic α-helix of NHE1 are inserted into the hydrophobic cleft in such a way that they face the C- and N-lobes of CHP2, respectively (Figure 3A). This cleft constitutes the region that traps the cytoplasmic α-helix of NHE1 and maintains the stability of the complex by means of hydrophobic interactions. The contact area between CHP2- and NHE1 peptide is 1466 $Å^2$, which accounts for 13.0

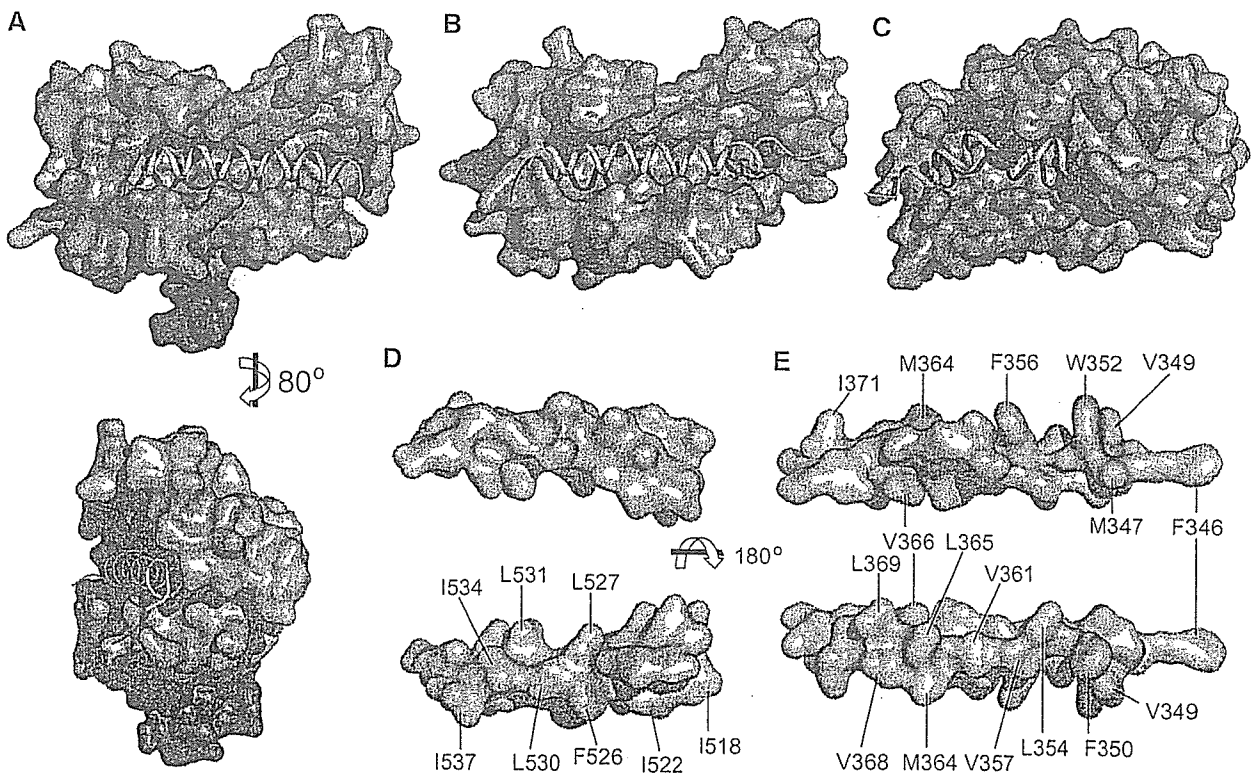

Figure 3 Target specificity of hydrophobic cleft. (**A–C**) Surface features of CHP2, CNB, and KChP1 are presented together with α-helices of target peptides, respectively. In CHP2, front (*upper*) and side (*lower*) views are shown. The N- and C-lobes are colored *light blue* and *light green*, while the CHP-unique region is colored *red*. (**D, E**) Surface view of NHE1 (*left*) and CNA (*right*) peptides, respectively. The *upper* panels indicate the side facing outside the cleft and the *lower* panels represent the side facing the cleft. Hydrophobic residues are colored *yellow*.

and 59.8% of the total surface areas, respectively, implying that a large area is used for interaction between the two molecules. The NHE1 peptide (Arg516–His540) solved in this structure contains different hydrophobic residues, all of which face toward the hydrophobic cleft of CHP2 (Figure 3D). Ile518, Ile522, Phe526, Leu527, and Leu530 are accommodated into the cavity formed by hydrophobic residues provided mainly from the C-lobe of CHP2, whereas Leu531, Ile534, and Ile537 are inserted into the cavity formed mainly by the N-lobe of CHP2 (Figure 4A and B). All hydrophobic side chains of the NHE1 peptide, with the exception of Ile518, make van der Waals contacts with side chain atoms from many hydrophobic residues of CHP2. For example, side chain atoms of Ile534 make van der Waals contacts with those of Leu57, Ile66, Phe70, Val86, Leu87 Phe90, Tyr118, and Ile192 of CHP2 (Figure 4C), while side chain atoms of Leu527 make interactions with those of Ala119, Leu181, Val186, Met184, and Met190 (Figure 4A). In addition to hydrophobic interactions, hydrogen bonds strengthen the association between CHP2 and NHE1 peptide. In the N-lobe of CHP2, the guanidinium group of Arg30 makes hydrogen bonds with the main chain carbonyl oxygen of Gly539, while the guanidinium group of Arg34 makes hydrogen bonds with the main chain carbonyl oxygens of Asp536 and Ile537 (Figure 4B). These hydrogen bonds are very important for the C-terminal end of the NHE1 helix to fix to the edge of the hydrophobic cleft of CHP2. The conserved Gly539 residue of NHE1 would allow the following cytoplasmic stretch to leave the cleft by inducing clear bending of the NHE1 peptide (Figures 3A and 4B). Several other hydrogen bonds are also formed. The hydrogen bond between the imidazole group (Nδ) of His523 in NHE1 and the side chain oxygen of Tyr123 in CHP2 is particularly interesting because it is the only polar interaction in the hydrophobic surface of the cleft (Supplementary Figure 3). These polar interactions are important to determine the specificity and orientation of CHP2 toward the cytoplasmic α-helix of NHE1.

Although CNB and KChIP1 have similar hydrophobic clefts (Figure 3B and C), their size and shape are clearly different from those of CHP2. Interestingly, target peptides show sequence features that just fit to their clefts. While NHE1 peptide shows a uniform distribution of hydrophobic residues all facing toward the cleft of CHP2 (Figure 3D), CNA contains more hydrophobic residues that face toward both the CNB crevice and the outside (Figure 3E). In addition, CNA peptide contains four aromatic residues (Phe346, Phe350, Trp352, and Phe356) in the N-terminus, which are accommodated in corresponding hydrophobic cavities in the C-lobe of CNB, whereas NHE1-peptide contains only one aromatic residue (Phe526) located in the central part of CHP2. These observations suggest that highly selective fitting of each peptide to its corresponding crevices may be caused by differences in the distribution of hydrophobic residues of the target peptides and in the shape of the cleft formed by α-helices of EF-hands.

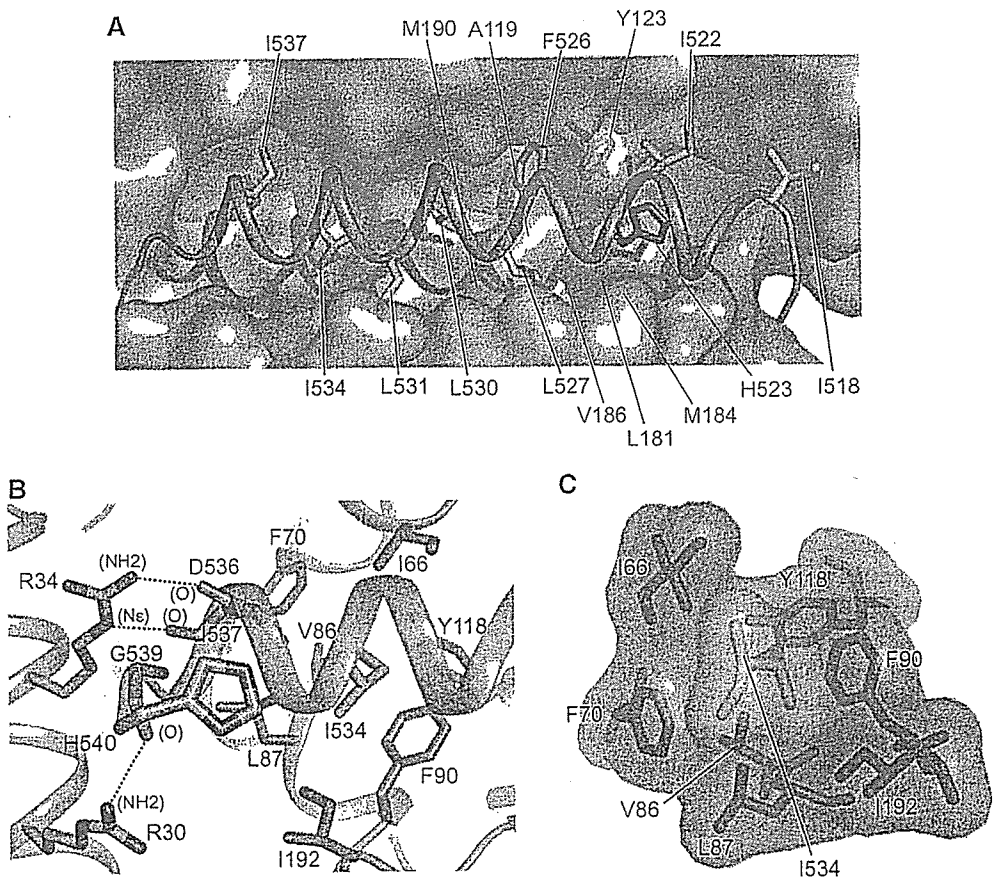

Figure 4 Closeup view showing the interaction between CHP2 and NHE1-peptide. (A) The NHE1-peptide backbone is shown in *magenta*, while hydrophobic side chains are shown in *yellow*. The hydrophobic pocket surrounding Leu527 is marked in *red*. His523 of NHE1 and Tyr123 of CHP2 are marked in *blue*. (B) Closeup view showing interaction between the N-lobe of CHP2 and the C-terminus of NHE1-peptide. (C) Ile534 is accommodated into the hydrophobic pocket produced by residues mainly in the N-lobe of CHP2.

Effect of mutations on interaction between NHE1 and CHP2 in cells

The present structure indicated that the correct CHP-binding domain of NHE1 consists of the region from aa 516–540, extended by 10 residues toward the C-terminus of the region (aa 510–530), as predicted previously (Pang *et al*, 2001). This prompted us to mutate residues in this extended region of NHE1 interacting with the N-lobe of CHP2. We mutated the Ile534 and Ile537 residues of NHE1 into charged residues (Lys or Asp) and stably expressed these mutants in exchanger-deficient PS120 cells. These mutants were expressed in the plasma membrane (as indicated by the existence of surface-expressed mature NHE1 in Supplementary Figure 4). We examined the interactions of these mutants with CHP2 by assessing whether stably transfected green fluorescent protein (GFP)-tagged CHP2 was localized to the plasma membrane. As shown in Figure 5A, most of the CHP2 was localized to the plasma membrane of cells expressing the wild-type NHE1 but not in nontransfected PS120 cells (not shown; see Pang *et al*, 2001), indicating a strong interaction. Of note, in most cells expressing the wild-type NHE1 almost no GFP-fluorescence was detected in the intracellular space (Figure 5A), despite the accumulation of immature NHE1 in the intracellular membranes under forced expression (data not shown), suggesting that CHP2 interacts predominantly with mature NHE1 in the plasma membrane. This was further confirmed by the finding that almost no immature NHE1 co-immunoprecipitated with CHP2 (Supplementary Figures 1 and 4). In contrast to the wild-type NHE1, the plasma membrane localization of CHP2 was almost completely abolished when transfected into cells expressing the NHE1 mutants, I534K, I534D and I537K (Figure 5, and also D for summarized data), indicating that these mutations drastically reduced the affinity for interaction with CHP2.

Furthermore, as expected, the plasma membrane localization of CHP2 was also markedly reduced in cells expressing the wild-type NHE1 when Leu87 or Tyr118 of CHP2 was changed to Lys (Figure 5C and D), indicating that these mutants are not able to replace completely endogenous CHP1 bound to NHE1. As the expression of GFP-tagged CHP2 was approximately 10-fold higher than that of endogenous CHP1 (data not shown), these results suggest that these mutations would reduce the affinity for interaction with NHE1 at least one-order of magnitude. Similar analysis was performed with mutation of the Arg residues (Arg30 and Arg34) in the N-terminal α-helix of CHP2. The plasma membrane localization of CHP2 was abolished when these two residues were simultaneously changed to Glu (Figure 5C and D), while it was still partially preserved when either Arg residue alone was changed to Glu. Similar results were also obtained for the NHE1/CHP2 interaction in a co-immunoprecipitation experiment (Supplementary Figure 4). Thus, the hydrophobic and polar interactions involving these residues would be important in determining the strong and highly specific association between NHE1 and CHP2, Furthermore, in addition to the C-lobe, the N-lobe of CHP2 plays a crucial role in the tight interaction with NHE1, suggesting that our crystal structure reflects the interaction between native NHE1 and CHP2 molecules expressed in cells. On the other hand, structure determination indicated the existence of a unique protruding region in CHP2. In contrast to mutations of residues involving formation of the cleft, a mutant with deletion of this CHP-unique region (Δ94–104) was mostly localized to the plasma membrane of cells expressing wild-type NHE1 (Figure 5C), indicating that deletion did not disrupt the interaction of CHP2/NHE1. Hence, as also predicted from structure, the CHP-unique region was not involved in the interaction between CHP2/NHE1. The 10 N-terminal residues of CHP2 were also found not to be involved in the interaction, as indicated by the plasma membrane localization of ΔN10 (Figure 5C).

Functional consequence of mutations

We measured the NHE activity in cells expressing mutant exchangers. Figure 6A demonstrates the pH_i-dependence of EIPA-sensitive $^{22}Na^+$-uptake activity. While the wild-type NHE1 exhibited high $^{22}Na^+$-uptake activity, with pK ~6.5 for pH_i (Hill coefficient, ~1.7), the activity of mutant exchangers, I534D, I534K and Ile537, which lack CHP-binding was very low (see Supplementary Table I for kinetic parameters). The inhibitory effect of the mutations was characterized by changes in two parameters: (i) a drastic reduction of maximal $^{22}Na^+$-uptake activity (V_{max}) at acidic pH_i, and (ii) a large acidic shift of the pH_i-dependence of uptake (>0.6 pH units) (see Figure 6A, inset for normalized activity). We then compared the pH_i-dependence of $^{22}Na^+$-uptake in cells co-expressing NHE1 with GFP-tagged CHP2 or its deletion mutant Δ94–104, which preserves interaction with CHP. Interestingly, expression of Δ94–104 significantly shifted the pH_i-dependence of uptake towards acidic pH_i (~0.2 pH unit) without any change in V_{max}, while it preserved the cooperative pH_i dependence, with a Hill coefficient ~1.5 (Figure 6B, see also inset for the sigmoidal internal H^+ dependence), suggesting that the CHP-unique region is involved in regulation of pH-sensing of NHE1. In general, the sigmoidal H^+-dependence has been interpreted as exhibiting involvement of at least two H^+-binding sites: H^+-transport and H^+-regulatory sites in NHE (Wakabayashi *et al*, 1997). To examine the effect of deletion of a CHP-specific region on the H^+-regulatory site, we measured the reverse reaction of NHE1, that is, $^{22}Na^+$ efflux coupled to H^+-influx. If we assume that NHE1 catalyzes a counter-transport reaction only involving the transport site, intracellular acidification should result in inhibition of $^{22}Na^+$ efflux due to cytosolic Na^+/H^+ competition. In contrast to this thermodynamically expected inhibition, modest acidification from 7.5 to 7.2 dramatically stimulated the rate of EIPA-inhibitable $^{22}Na^+$ efflux in cells co-expressing the wild-type NHE1 and CHP2 (Figure 6D), suggesting that protonation of H^+-regulatory sites activated NHE1 (Figure 6C), as reported in detail, previously (Aronson *et al*, 1982; Wakabayashi *et al*, 2003a). Consistent with the acidic shift of pH_i-dependence of $^{22}Na^+$ uptake, we observed that deletion of a CHP-unique region significantly reduced the rate of $^{22}Na^+$ efflux (Figure 6D). EIPA-sensitive fraction of $^{22}Na^+$ efflux at pH_i 7.2 during the initial 3 min was reduced to ~30% upon expression of Δ94–104, suggesting that the affinity of the H^+-regulatory site for H^+ decreased upon deletion of this region.

Discussion

In the present study, we solved the first crystal structure of the CHP2/NHE1-peptide complex at 2.7 Å. This structure provides detailed information regarding the interaction between

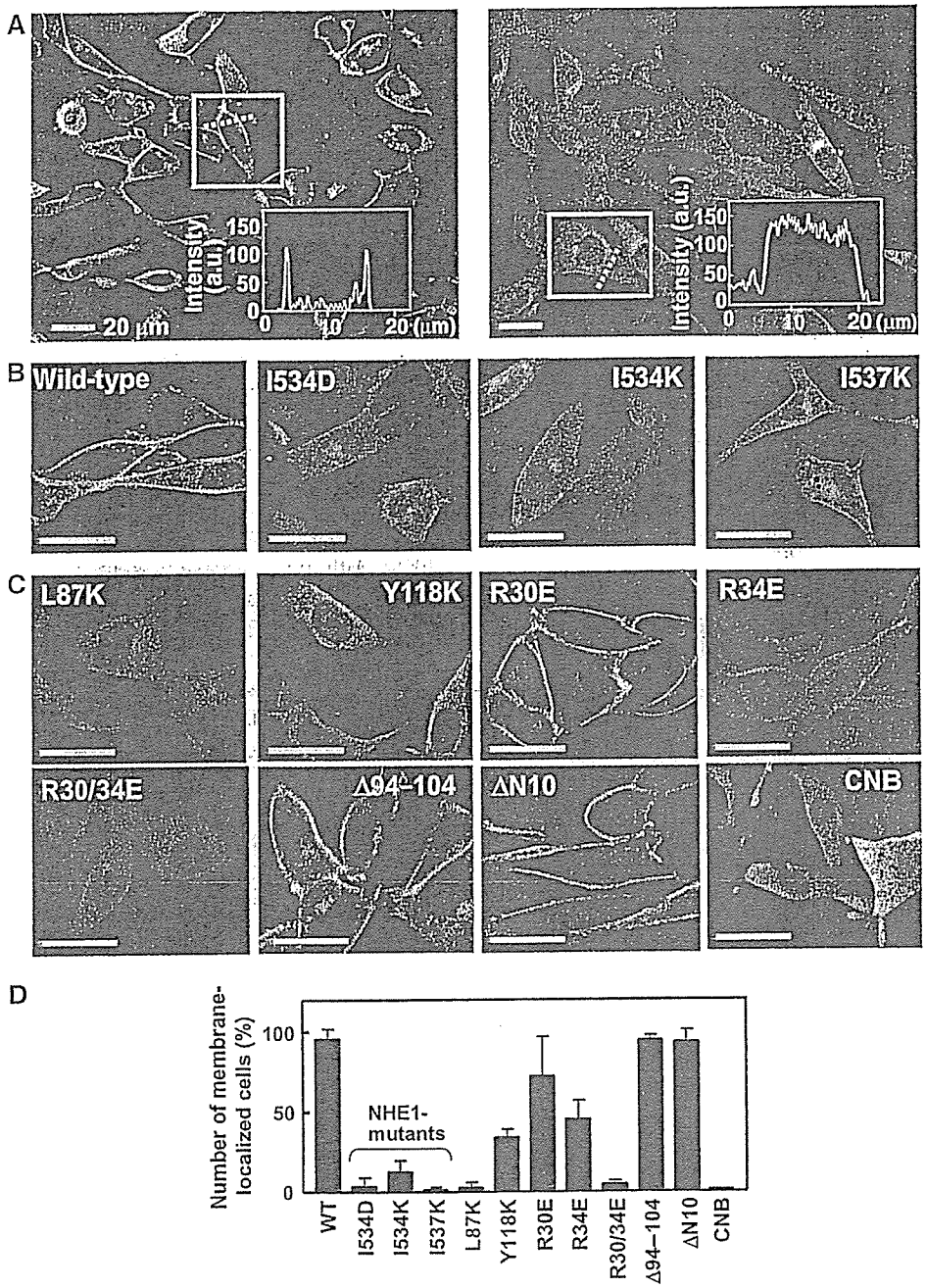

Figure 5 Effects of mutations on the interaction between NHE1 and CHP2 in cells. (A) Low magnification confocal images of cells coexpressing GFP-tagged CHP2 and the wild-type (*left*) or I537K (*right*) mutant exchangers. Inset shows the intensity profile of GFP fluorescence along the dotted line in a marked cell. In most cells expressing the wild-type NHE1 but not I537K, strong fluorescent signals were detected at the cell edge. (B) Subcellular localization of CHP2 expressed in cells. GFP-tagged CHP2 was coexpressed in cells stably expressing the wild-type or mutant NHE1 variants and GFP-fluorescence was observed by confocal microscopy. (C) Subcellular localization of mutant CHP2. GFP-tagged CHP2 mutants were expressed in cells stably expressing the wild-type NHE1. Eleven residues from Glu94 to Lys104 of CHP2 were deleted in Δ94–104, while the 10 N-terminal residues from Met1 to Val10 were deleted in ΔN10. For one control experiment, GFP-tagged human CNB was expressed in NHE1-transfectants. (D) Summary data for membrane localization of GFP-tagged CHP2. Intensity profile analysis was performed on confocal images as shown in (A). The number of cells with strong fluorescence signal at the cell edge (at least three times more than the average of fluorescence in the internal cell region) was counted. Data are expressed as the mean±s.d. from 6–8 images (total cell number analyzed, 99–341).

NHE1 and CHP: (i) the interaction with NHE1 occurs in a hydrophobic cleft encompassing the N- and C-lobes of CHP2, (ii) this interaction occurs by extensive Van der Waals contact between hydrophobic residues, as well as by some specific hydrogen bonds, (iii) the interacting region of NHE1 forms an α-helix which bends at a conserved Gly539 and (iv) two domains of CHP2 are connected by a large flexible CHP-unique region. These features strengthened our previous functional study (Pang *et al*, 2001, 2002, 2004) from structural aspects and at the same time provided new information to be addressed regarding the function of NHE1.

A unique feature of interaction between CHP and NHE

Structure comparison among Ca^{2+}-binding proteins provided valuable information regarding the target specificity of CHP1/2 proteins. Although the crystal structure of CNB/CNA com-

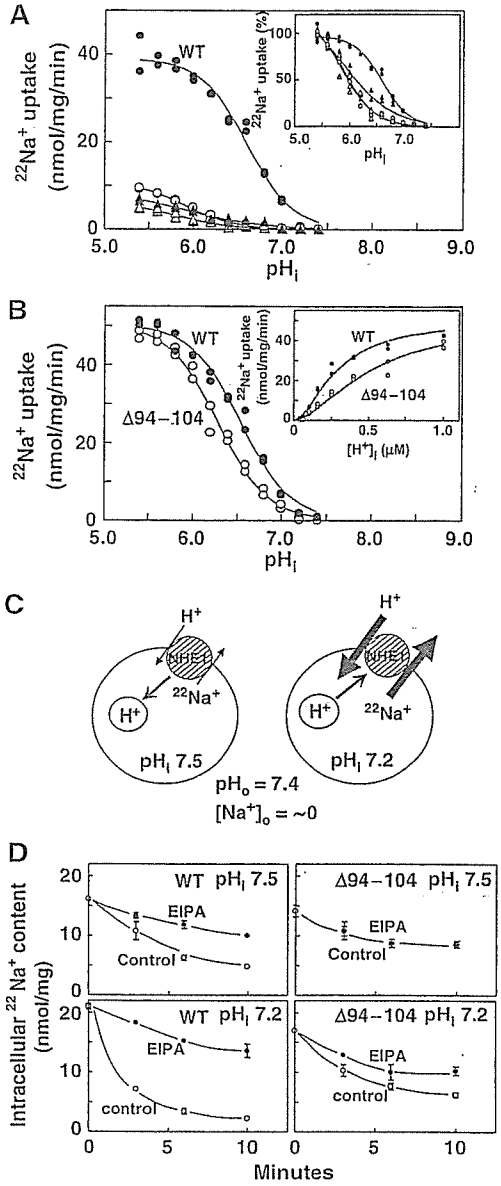

Figure 6 Effect of mutations on the exchange activity. (**A**), pH$_i$-dependence of EIPA-sensitive $^{22}Na^+$-uptake in cells expressing wild-type NHE1 (●) or CHP binding-defective mutants, I534D (○), I534K (▲) and I537K (△). pH$_i$ was clamped at various values with K^+/nigericin. Data were fitted to Hill equations with the kinetic parameters shown in Supplementary Table I and plotted after normalization by the maximal activity at pH$_i$ = 5.4 (*inset*). (**B**) pH$_i$-dependence of EIPA-sensitive $^{22}Na^+$-uptake in cells co-expressing wild-type NHE1 and GFP-tagged CHP2 (●) or deletion mutant Δ94–104 of CHP2 (○). Data were fitted to Hill equations with the kinetic parameters shown in Supplementary Table I. The $^{22}Na^+$-uptake activity was also plotted against intracellular H^+ concentration up to 1 μM (*inset*). (**C**) Schematic drawing of $^{22}Na^+$-efflux protocol. The efflux experiment was done in $^{22}Na^+$-loaded, pH$_i$-clamped cells at extracellular pH 7.4. At lower pH$_i$ $^{22}Na^+$ efflux would be accelerated by H^+ binding to the regulatory site, while at high pH$_i$ it would be inhibited by H^+-release from the regulatory site. (**D**) Time courses of $^{22}Na^+$ efflux. Cells were loaded with $^{22}Na^+$ and at the same time pH$_i$-clamped at pH$_i$ 7.5 or 7.2. After removal of the radioactive solution, cells were exposed to the nonradioactive solutions with or without 0.1 mM EIPA. Data are expressed as the mean ± s.d. of three determinations. Error bars are sometimes smaller than symbol sizes.

plex (Kissinger *et al*, 1995) revealed a similar mode of interaction through its hydrophobic groove, comparison between the hydrophobic clefts of CHP2 and CNB showed several different structural features (Figure 3A and B). In addition, there is a marked difference in the distribution of hydrophobic residues between NHE1- and CNA peptides (Figure 3D and E). Such local structural differences between CHP2 and CNB, together with differences between target peptide sequences, may explain the selectivity of CHP1/2 toward the NHE members and of CNB toward CNA, and led us to predict that NHE1 may not be a target for CNB. In fact, we observed that GFP-tagged CNB was not localized to the plasma membrane when co-expressed with NHE1 (Figure 5C). On the other hand, since the C-lobe of KChIP1 is occupied by the α10 helix of itself (Figure 3C), KChIP1 associates with its target K^+-channel molecule only through the N-lobe (Zhou *et al*, 2004). Crystal structures have been also solved for several other Ca^{2+}-binding proteins belonging to the NCS family: recoverin (Flaherty *et al*, 1993), NCS-1 (Bourne *et al*, 2001), neurocalcin (Vijay-Kumar and Kumar, 1999), AtCBL2 (Nagae *et al*, 2003), and CIB (Gentry *et al*, 2005). Although all these proteins have hydrophobic crevices that would interact with the target molecules, the sizes and shapes of these crevices are clearly different. In contrast to calmodulin, which is able to interact with a variety of proteins with broad specificity, target molecules for CNB and NCS family proteins appear to be limited. Structural differences in the hydrophobic cleft together with highly specific polar interactions would enable the diverse array of Ca^{2+} binding proteins belonging to these families to associate selectively and tightly with the target molecules.

Of note, the N-lobe of CHP2 associates tightly with the C-lobe within a large area (Figure 3A). The contact area between the two domains is 1066 Å^2, accounting for 16.6 and 15.2% of the total surface areas of the N- and C-lobes, respectively. Such interaction between the two lobes would result in the formation of a rigid cleft structure independent of the target peptide. In fact, the structure of the hydrophobic cleft of CHP2 is very similar to that of target-free CHP1 (Naoe *et al*, 2005). In addition, the N-lobe of CHP2 does not contain the methionine residue that was suggested to produce plasticity allowing fine-tuning toward various target molecules in calmodulin (Osawa *et al*, 1998). Therefore, NHE1-peptide would enter the preformed cleft, rather than the interaction being caused by a conformational change in the cleft. This target-independent rigid structure would allow the CHP-unique region to exert specific physiological functions, beyond a role as a connecting linker. This is in contrast to calmodulin the flexible liker region between the two domains of which is known to act as a hinge when it recognizes various target molecules (Zhang *et al*, 1995).

CHP1/2 is myristoylated and has two Ca^{2+} ions. However, these properties are different from those of other CNB and NCS family proteins. Mutation of CHP1 that prevents myristoylation has no apparent effect on plasma membrane expression or the exchange activity of NHE1. Therefore, myristoylation of CHP1/2 would not be required for the plasma membrane translocation of NHE1 or for the exchange activity (Pang *et al*, 2001, 2004), in contrast to KChIP1 (An *et al*, 2000). In addition, unlike recoverin, which undergoes the Ca^{2+}-myristoyl switch (Ames *et al*, 1997), the myristoyl moiety of CHP1/2 would always be exposed outside the core structure upon interaction with NHE1 and probably embedded in the plasma membrane. Thus, the physiological function of myristoylation is still unknown. On the other hand,

unlike many other Ca^{2+}-binding proteins, only EF3 and EF4 of CHP1/2 are able to coordinate Ca^{2+} ions. Removal of Ca^{2+} with a Ca^{2+}-chelator significantly reduced the interaction between NHE1 and CHP2 (Supplementary Figure 1) and a double mutation of EF3 and EF4 of CHP1 abolished the interaction with NHE1 (Pang *et al*, 2004). Furthermore, the Ca^{2+} affinity of CHP1 increases markedly (40-fold) upon interaction with NHE1 (Pang *et al*, 2004). These findings suggest that Ca^{2+}-binding sites and the hydrophobic cleft are structurally coupled, that is, the Ca^{2+}-bound conformation of EF-hands is required for the formation of the appropriate structure of the hydrophobic cleft for the interaction with NHE1. By analogy with calmodulin (Zhang *et al*, 1995), we consider that Ca^{2+} binding opens the hydrophobic pockets of EF-hands so that the residues of the C-lobe can fit into the hydrophobic cleft. However, such Ca^{2+}-induced conformational changes of CHP1/2 bound to NHE1 would not occur physiologically in cells, since the Ca^{2+} affinity for such a complex would be extremely high, that is, K_d for Ca^{2+} ($2 \sim 3$ nM) is much less than the physiological cytosolic Ca^{2+} concentration (0.1–1 μM) (Supplementary Figure 1 and see also Pang *et al*, 2004). Hence, we suggest that Ca^{2+} bound to EF-hands plays a structural role in stabilizing the hydrophobic cleft of CHP1/2. In the case of NHE1, Ca^{2+}-induced activation would take place on another Ca^{2+}-binding protein CaM, which binds to the middle of the cytoplasmic domain of NHE1 (Bertrand *et al*, 1994; Wakabayashi *et al*, 1994).

Implications for roles of CHP in NHE function

We demonstrated that Ile534 and Ile537 in NHE1 are critical residues for interaction with CHP2 (Figure 5). Mutations of these residues resulted in a disruption of NHE1 function, as characterized by a drastic reduction of the maximal exchange activity and a large acidic shift of the pH_i-dependence of exchange (Figure 6). This is consistent with our previous findings obtained by simultaneous mutation of four hydrophobic residues (Phe526, Leu527, Leu530 and Leu531) of NHE1, substituted with Gln or Arg (Pang *et al*, 2001, 2004). On the other hand, deletion of the CHP-unique region (Δ94–104) significantly reduced the physiological exchange activity by inducing an acidic shift of the pH_i-dependence of $^{22}Na^+$-uptake (Figure 6B) and inhibited the rate of $^{22}Na^+$ efflux (Figure 6D), while preserving the maximal activity at acidic pH_i (Figure 6B), suggesting that this region functions as an important segment controlling pH_i by interacting with NHE1. Based on these findings, we propose that CHP1/2 plays two important roles in the function of NHE1. First, CHP functions as an obligatory subunit, which activates almost non-functional NHE1 by tightly associating with its cytoplasmic domain via the hydrophobic cleft. This activation is characterized by increases in both V_{max} and the H^+-affinity. Secondly, CHP would participate in the delicate pH_i regulation of NHE1 through the CHP-unique region, which is involved in modulation of the H^+-affinity, but not V_{max}.

We predict that CHP may stabilize the structure of the juxtamembrane domain by inducing a stable α-helix, thereby preserving NHE1 in the functional conformation. Indeed, circular dichroism measurements indicated that the CHP-free, CHP-binding peptide has no secondary structure in aqueous solution (data not shown), although we do not exclude the possibility that this region is folded within the entire structure. On the other hand, the dominant-negative effect of Δ94–104 raises the interesting possibility that it may regulate the pH_i-sensing by interacting with some regions of NHE1. We observed that NHE1 and CHP2 crosslinked with each other through IL5 of NHE1 and the CHP-unique region (Supplementary Figure 5), suggesting that these regions in the two proteins are located in accessible positions beneath the membranes. Since, similar to Δ94–104 of CHP2, mutation of Arg440 in IL5 results in a large acidic shift of the pH_i-dependence of $^{22}Na^+$-uptake and efflux (Wakabayashi *et al*, 2003a, b), we consider that IL5 would be one of targets for the CHP-unique region. Although we do not have direct evidence, IL4 may be another target region because mutation of Arg327 in IL4 has also been reported to lead to a similar functional defect of NHE1(Lacroix *et al*, 2004). Activation of $^{22}Na^+$ efflux by cytosolic acidification predicted the existence of an additional H^+-regulatory site(s) (Figure 6C and D; Aronson *et al*, 1982; Wakabayashi *et al*, 2003a). This phenomenon does not appear to be fully explained by the recent allosteric model, in which only H^+-transport sites are assumed to participate in the cooperative H^+-activation of NHE1 (Lacroix *et al*, 2004). We speculate that multiple charged residues in loops of NHE1, as well as in CHP1/2, may serve as 'pH-sensor' sites, which accept protons, although further investigation will be required to support this concept. The recently reported crystal structure of the bacterial Na^+/H^+ antiporter, NhaA, predicted that modification of charged residues provided by cytoplasmic loops may activate NhaA by exposing the cation transport site via reorientation of transmembrane helices (Hunte *et al*, 2005).

Finally, it should be noted that the relatively long juxtamembrane domain (aa 503–595) of NHE1 is essential for the physiological exchange activity (Ikeda *et al*, 1997; Wakabayashi *et al*, 1997), although we focused on the CHP-binding domain in the present study. Similar to the CHP-binding region, it is likely that the region covering aa 503–595 forms a stable structure by interacting with several accessory factors. Indeed, this region appears to be structurally unstable when expressed in *Escherichia coli* or in mammalian cells as a single polypeptide, as evidenced by its rapid degradation (unpublished observation), despite the fact that the whole cytoplasmic domain can be easily expressed in these cells. In addition, a previous study (Aharonovitz *et al*, 2000) indicated that positively charged clusters (aa 509–516 and aa 552–560 in human NHE1) interact with polyphosphoinosides (PIP_2). These regions were also reported to interact with ezrin, although interaction with ezrin is independent of the exchange activity (Denker *et al*, 2000; Baumgartner *et al*, 2004). Furthermore, we recently reported that a region (aa 560–580) of NHE1 may be involved in dimeric interactions (Hisamitsu *et al*, 2004). Such homotypic interactions may provide another way for stabilization of the structure, as deletion of aa 560–580 resulted in a marked reduction of exchange activity by inducing the acidic shift of pH_i-dependence (Hisamitsu *et al*, 2004). These findings raise the possibility that multiple homotypic and heterotypic interactions may induce stabilization of the juxtamembrane region and thereby form a substructure regulating the exchange activity. Clearly, CHP is an obligatory member in such regulatory machinery of NHE1.

In summary, we first determined the crystal structure of CHP2 complexed with its binding region in NHE1 and

clarified the mechanism by which CHP tightly and specifically associates with plasma membrane members of the NHE family. Structure-based mutagenesis revealed the physiological importance of CHP in pH_i regulation by NHE1. Most Ca^{2+}-binding proteins have long been recognized to function as Ca^{2+}-sensors or Ca^{2+}-buffers. In contrast to this general understanding, CHP does not appear to be a Ca^{2+}-sensor, but rather acts as a critical regulator of pH-sensing activity in the exchangers, presumably mediated by the CHP-unique region. The results of the present study cast new light on a unique function of CHP that was not reported in other canonical EF-hand Ca^{2+}-binding proteins.

Materials and methods

Protein expression and purification

The complex of human full-length CHP2 (aa 1–196) with its binding region (aa 503–545) in NHE1 was expressed and purified essentially as described previously (Pang *et al*, 2004; Ben Ammar *et al*, 2005).

Crystallization and data collection

Crystals of the complex CHP2/NHE1-peptide were grown using the sitting-drop vapor diffusion technique at 20°C. To obtain the best crystal quality, 1.5 µl of the protein complex solution containing 20 mM yttrium chloride was mixed with 1 µl of the reservoir solution containing 200 mM ammonium acetate, 100 mM Bis–Tris, pH 5.5, and 25% (w/v) PEG 3350 as described previously (Ben Ammar *et al*, 2005). Crystals were not obtained without adding yttrium chloride to the crystallization solution, suggesting that yttrium ion(s) were involved in crystal packing. Therefore, taking advantage of the yttrium ion(s) in the crystal, we collected multiple wavelength data sets around the absorption edge of the yttrium atom at SPring-8 beamline BL44B2. A high-resolution single-wavelength data set ($\lambda = 1$ Å) was collected at beamline BL41XU at SPring-8. The statistics of the data collection are summarized in Table I.

Structural determination and refinement

The structure of the CHP2/NHE1-peptide complex was determined by MAD phasing. The program SOLVE (Terwilliger and Berendzen, 1999) was used to determine two yttrium positions and the initial phases with a figure of merit of 0.43 at 3.1 Å resolution. The program RESOLVE (Terwilliger, 2000) improved the phases and produced the initial polyalanine model, which covered 65% of the residues of the CHP2/NHE1-peptide complex. The model was built with TURBO-FRODO and refined against the high resolution data set to 2.7 Å using CNS (Brunger *et al*, 1998), and subsequent rounds of model building and refinement produced the final structural model. The residues in the final model lie in 87.2% in the most favorable and 12.8% in the additionally allowed regions of the Ramachandran plot. Refinement statistics are summarized in Table I. Figures 2–4 were generated using PyMOL graphing software (http://www.pymol.org).

Construction of mammalian expression plasmids

The plasmid carrying the cDNA encoding NHE1 containing unique restriction sites cloned into the mammalian expression vector pECE was described previously (Wakabayashi *et al*, 1992). Construction of plasmids for various NHE1 or CHP2 mutants tagged with GFP or hemagglutinin (HA) epitope YPYDVPDYAS was carried out by a PCR-based strategy as described previously (Wakabayashi *et al*, 2000). PCR fragments were digested and cloned into the appropriate restriction sites of vectors pECE or pGEFP-N1 (Clontech, Palo Alto, CA) for NHE1 or CHP2, respectively.

Cell culture and plasmid transfection

The exchanger-deficient cell line PS120 (Pouyssegur *et al*, 1984) and corresponding transfectants were maintained in Dulbecco's modified Eagle's medium containing 25 mM $NaHCO_3$ and supplemented with 5% (v/v) fetal calf serum. All cDNA constructs were transfected into PS120 cells with Lipofectamine 2000 (Invitrogen), and stable clones for NHE1 and its mutant constructs were selected by repetitive H^+-killing selection procedures as described previously (Wakabayashi *et al*, 1992). GFP-tagged CHP2 variants were stably expressed in cells expressing various mutant NHE1 proteins and fluorescence images were taken under a confocal fluorescence microscope (BioRad).

Measurement of $^{22}Na^+$-uptake and $^{22}Na^+$-efflux activities

$^{22}Na^+$-uptake activity was measured by the K^+/nigericin pH_i clamp method as described previously (Ikeda *et al*, 1997). Data were simulated by fitting the values to the sigmoidal dose–response equation, rate of EIPA-sensitive $^{22}Na^+$-uptake $= V_{max}/(1 + 10^{(\log(pK - pH_i)^n)})$ (pK, pH_i giving half maximal $^{22}Na^+$ uptake; n, Hill coefficient), using the simulation program included in Graphpad Prizm (Microsoft Corp., Redmond, WA). $^{22}Na^+$ efflux was measured as described previously (Wakabayashi *et al*, 2003a). Briefly, serum-depleted cells in 24-well dishes were loaded with $^{22}Na^+$ by preincubating them for 30 min at 37°C in chloride/KCl medium containing 1 mM $^{22}NaCl$ (37 kBq/ml) and at the same time pH_i-clamped at 7.5 or 7.2 in presence of 5 µM nigericin. The radioactive solution was removed and $^{22}Na^+$ efflux was initiated by adding the nonradioactive medium. At the times indicated in figures, cells were rapidly washed four times with ice-cold PBS and the remaining ^{22}Na-radioactivity in the cells was counted.

Coordinates

Coordinates and structure factor amplitudes have been deposited in the Protein Data Bank with accession code 2BEC.

Supplementary data

Supplementary data are available at *The EMBO Journal* Online.

Acknowledgements

We thank the staff at beamline BL44B2 and BL41XU, SPring-8, for support with data collection, Dr Sugawara and Dr Miyano (RIKEN Harima Institute) for fruitful discussion, Dr Tomoe Y Nakamura for critical reading of manuscript, and Dr Tianxiang Pang for the initial participation in this study. This work was supported by Grant nano-001 for Research on Advanced Medical Technology from the Ministry of Health, Labor, and Welfare of Japan and Grant-in-Aid for Priority Areas 13142210 for Scientific Research from the Ministry of Education, Science, and Culture of Japan. YBA is a Japan Society for the Promotion of Science (JSPS) Postdoctoral Fellow.

References

Aharonovitz O, Zaun HC, Balla T, York JD, Orlowski J, Grinstein S (2000) Intracellular pH regulation by Na(+)/H(+) exchange requires phosphatidylinositol 4,5-bisphosphate. *J Cell Biol* 150: 213–224

Ames JB, Ishima R, Tanaka T, Gordon JI, Stryer L, Ikura M (1997) Molecular mechanics of calcium-myristoyl switches. *Nature* 389: 198–202

An WF, Bowlby MR, Betty M, Cao J, Ling HP, Mendoza G, Hinson JW, Mattsson KI, Strassle BW, Trimmer JS, Rhodes KJ (2000) Modulation of A-type potassium channels by a family of calcium sensors. *Nature* 403: 553–556

Aronson PS, Nee J, Suhm MA (1982) Modifier role of internal H+ in activating the Na+-H+ exchanger in renal microvillus membrane vesicles. *Nature* 299: 161–163

Barroso MR, Bernd KK, DeWitt ND, Chang A, Mills K, Sztul ES (1996) A novel Ca2+-binding protein, p22, is required for constitutive membrane traffic. *J Biol Chem* 271: 10183–10187

Baumgartner M, Patel H, Barber DL (2004) Na(+)/H(+) exchanger NHE1 as plasma membrane scaffold in the assembly of signaling complexes. *Am J Physiol Cell Physiol* 287: C844–C850

Ben Ammar Y, Takeda S, Sugawara M, Miyano M, Mori H, Wakabayashi S (2005) Crystallization and preliminary crystal-

lographic analysis of the human calcineurin homologous protein CHP2 bound to the cytoplasmic region of the Na+/H+ exchanger NHE1. *Acta Crystallograph Sect F* **61**: 956–958

Bertrand B, Wakabayashi S, Ikeda T, Pouyssegur J, Shigekawa M (1994) The Na+/H+ exchanger isoform 1 (NHE1) is a novel member of the calmodulin-binding proteins. Identification and characterization of calmodulin-binding sites. *J Biol Chem* **269**: 13703–13709

Bourne Y, Dannenberg J, Pollmann V, Marchot P, Pongs O (2001) Immunocytochemical localization and crystal structure of human frequenin (neuronal calcium sensor 1). *J Biol Chem* **276**: 11949–11955

Brunger AT, Adams PD, Clore GM, DeLano WL, Gros P, Grosse-Kunstleve RW, Jiang JS, Kuszewski J, Nilges M, Pannu NS, Read RJ, Rice LM, Simonson T, Warren GL (1998) Crystallography & NMR system: a new software suite for macromolecular structure determination. *Acta Crystallogr D* **54** (Part 5): 905–921

Counillon L, Pouyssegur J (2000) The expanding family of eucaryotic Na(+)/H(+) exchangers. *J Biol Chem* **275**: 1–4

Denker SP, Huang DC, Orlowski J, Furthmayr H, Barber DL (2000) Direct binding of the Na–H exchanger NHE1 to ERM proteins regulates the cortical cytoskeleton and cell shape independently of H(+) translocation. *Mol Cell* **6**: 1425–1436

Engelhardt S, Hein L, Keller U, Klambt K, Lohse MJ (2002) Inhibition of Na(+)-H(+) exchange prevents hypertrophy, fibrosis, and heart failure in beta(1)-adrenergic receptor transgenic mice. *Circ Res* **90**: 814–819

Flaherty KM, Zozulya S, Stryer L, McKay DB (1993) Three-dimensional structure of recoverin, a calcium sensor in vision. *Cell* **75**: 709–716

Gentry HR, Singer AU, Betts L, Yang C, Ferrara JD, Sondek J, Parise LV (2005) Structural and biochemical characterization of CIB1 delineates a new family of EF-hand-containing proteins. *J Biol Chem* **280**: 8407–8415

Gutierrez-Ford C, Levay K, Gomes AV, Perera EM, Som T, Kim YM, Benovic JL, Berkovitz GD, Slepak VZ (2003) Characterization of tescalcin, a novel EF-hand protein with a single Ca2+-binding site: metal-binding properties, localization in tissues and cells, and effect on calcineurin. *Biochemistry* **42**: 14553–14565

Hisamitsu T, Pang T, Shigekawa M, Wakabayashi S (2004) Dimeric interaction between the cytoplasmic domains of the Na+/H+ exchanger NHE1 revealed by symmetrical intermolecular cross-linking and selective co-immunoprecipitation. *Biochemistry* **43**: 11135–11143

Hunte C, Screpanti E, Venturi M, Rimon A, Padan E, Michel H (2005) Structure of a Na+/H+ antiporter and insights into mechanism of action and regulation by pH. *Nature* **435**: 1197–1202

Ikeda T, Schmitt B, Pouyssegur J, Wakabayashi S, Shigekawa M (1997) Identification of cytoplasmic subdomains that control pH-sensing of the Na+/H+ exchanger (NHE1): pH-maintenance, ATP-sensitive, and flexible loop domains. *J Biochem (Tokyo)* **121**: 295–303

Inoue H, Nakamura Y, Nagita M, Takai T, Masuda M, Nakamura N, Kanazawa H (2003) Calcineurin homologous protein isoform 2 (CHP2), Na+/H+ exchangers-binding protein, is expressed in intestinal epithelium. *Biol Pharm Bull* **26**: 148–155

Karmazyn M (2001) Role of sodium-hydrogen exchange in cardiac hypertrophy and heart failure: a novel and promising therapeutic target. *Basic Res Cardiol* **96**: 325–328

Kissinger CR, Parge HE, Knighton DR, Lewis CT, Pelletier LA, Tempczyk A, Kalish VJ, Tucker KD, Showalter RE, Moomaw EW, Gastinel LN, Habuka N, Chen X, Maldonado F, Barker JE, Bacquet R, Villafranca JE (1995) Crystal structures of human calcineurin and the human FKBP12-FK506-calcineurin complex. *Nature* **378**: 641–644

Lacroix J, Poet M, Maehrel C, Counillon L (2004) A mechanism for the activation of the Na/H exchanger NHE-1 by cytoplasmic acidification and mitogens. *EMBO Rep* **5**: 91–96

Lin X, Barber DL (1996) A calcineurin homologous protein inhibits GTPase-stimulated Na-H exchange. *Proc Natl Acad Sci USA* **93**: 12631–12636

Mailander J, Muller-Esterl W, Dedio J (2001) Human homolog of mouse tescalcin associates with Na(+)/H(+) exchanger type-1. *FEBS Lett* **507**: 331–335

Nagae M, Nozawa A, Koizumi N, Sano H, Hashimoto H, Sato M, Shimizu T (2003) The crystal structure of the novel calcium-binding protein AtCBL2 from *Arabidopsis thaliana*. *J Biol Chem* **278**: 42240–42246

Naoe Y, Arita K, Hashimoto H, Kanazawa H, Sato M, Shimizu T (2005) Structural characterization of calcineurin B homologous protein 1. *J Biol Chem* **280**: 32372–32378

Orlowski J, Grinstein S (2004) Diversity of the mammalian sodium/proton exchanger SLC9 gene family. *Pflugers Arch* **447**: 549–565

Osawa M, Swindells MB, Tanikawa J, Tanaka T, Mase T, Furuya T, Ikura M (1998) Solution structure of calmodulin-W-7 complex: the basis of diversity in molecular recognition. *J Mol Biol* **276**: 165–176

Pang T, Hisamitsu T, Mori H, Shigekawa M, Wakabayashi S (2004) Role of calcineurin B homologous protein in pH regulation by the Na+/H+ exchanger 1: tightly bound Ca2+ ions as important structural elements. *Biochemistry* **43**: 3628–3636

Pang T, Su X, Wakabayashi S, Shigekawa M (2001) Calcineurin homologous protein as an essential cofactor for Na+/H+ exchangers. *J Biol Chem* **276**: 17367–17372

Pang T, Wakabayashi S, Shigekawa M (2002) Expression of calcineurin B homologous protein 2 protects serum deprivation-induced cell death by serum-independent activation of Na+/H+ exchanger. *J Biol Chem* **277**: 43771–43777

Perera EM, Martin H, Seeherunvong T, Kos L, Hughes IA, Hawkins JR, Berkovitz GD (2001) Tescalcin, a novel gene encoding a putative EF-hand Ca(2+)-binding protein, Col9a3, and renin are expressed in the mouse testis during the early stages of gonadal differentiation. *Endocrinology* **142**: 455–463

Pouyssegur J, Sardet C, Franchi A, L'Allemain G, Paris S (1984) A specific mutation abolishing Na+/H+ antiport activity in hamster fibroblasts precludes growth at neutral and acidic pH. *Proc Natl Acad Sci USA* **81**: 4833–4837

Putney LK, Denker SP, Barber DL (2002) The changing face of the Na+/H+ exchanger, NHE1: structure, regulation, and cellular actions. *Annu Rev Pharmacol Toxicol* **42**: 527–552

Terwilliger TC (2000) Maximum-likelihood density modification. *Acta Crystallogr D* **56** (Part 8): 965–972

Terwilliger TC, Berendzen J (1999) Automated MAD and MIR structure solution. *Acta Crystallogr D* **55** (Part 4): 849–861

Vijay-Kumar S, Kumar VD (1999) Crystal structure of recombinant bovine neurocalcin. *Nat Struct Biol* **6**: 80–88

Wakabayashi S, Bertrand B, Ikeda T, Pouyssegur J, Shigekawa M (1994) Mutation of calmodulin-binding site renders the Na+/H+ exchanger (NHE1) highly H(+)-sensitive and Ca2+ regulation-defective. *J Biol Chem* **269**: 13710–13715

Wakabayashi S, Fafournoux P, Sardet C, Pouyssegur J (1992) The Na+/H+ antiporter cytoplasmic domain mediates growth factor signals and controls 'H(+)-sensing'. *Proc Natl Acad Sci USA* **89**: 2424–2428

Wakabayashi S, Hisamitsu T, Pang T, Shigekawa M (2003a) Kinetic dissection of two distinct proton binding sites in Na+/H+ exchangers by measurement of reverse mode reaction. *J Biol Chem* **278**: 43580–43585

Wakabayashi S, Hisamitsu T, Pang T, Shigekawa M (2003b) Mutations of Arg440 and Gly455/Gly456 oppositely change pH sensing of Na+/H+ exchanger 1. *J Biol Chem* **278**: 11828–11835

Wakabayashi S, Pang T, Su X, Shigekawa M (2000) A novel topology model of the human Na(+)/H(+) exchanger isoform 1. *J Biol Chem* **275**: 7942–7949

Wakabayashi S, Shigekawa M, Pouyssegur J (1997) Molecular physiology of vertebrate Na+/H+ exchangers. *Physiol Rev* **77**: 51–74

Zachos NC, Tse M, Donowitz M (2005) Molecular physiology of intestinal Na+/H+ exchange. *Annu Rev Physiol* **67**: 411–443

Zhang M, Tanaka T, Ikura M (1995) Calcium-induced conformational transition revealed by the solution structure of apo calmodulin. *Nat Struct Biol* **2**: 758–767

Zhou W, Qian Y, Kunjilwar K, Pfaffinger PJ, Choe S (2004) Structural insights into the functional interaction of KChIP1 with Shal-type K(+) channels. *Neuron* **41**: 573–586

Japanese Journal of Applied Physics
Vol. 45, No. 10A, 2006, pp. 8005–8009

Enhanced Magnification Angiography Using 20-μm-Focus Tungsten Tube

Toshiyuki ENOMOTO, Eiichi SATO[1], Yoshinobu SUMIYAMA, Katsuo AIZAWA[2], Manabu WATANABE, Etsuro TANAKA[3], Hidezo MORI[4], Hiroki KAWAKAMI[5], Toshiaki KAWAI[5], Takashi INOUE[6], Akira OGAWA[6] and Shigehiro SATO[7]

The 3rd Department of Surgery, Toho University School of Medicine, 2-17-6 Ohashi, Meguro-ku, Tokyo 153-8515, Japan
[1]*Department of Physics, Iwate Medical University, 3-16-1 Honchodori, Morioka 020-0015, Japan*
[2]*Tokyo Medical University [emeritus professor], 6-1-1 Shinjuku, Shinjuku-ku, Tokyo 160-8402, Japan*
[3]*Department of Nutritional Science, Faculty of Applied Bio-science, Tokyo University of Agriculture, 1-1-1 Sakuragaoka, Setagaya-ku, Tokyo 156-8502, Japan*
[4]*Department of Cardiac Physiology, National Cardiovascular Center Research Institute, 5-7-1 Fujishirodai, Suita, Osaka 565-8565, Japan*
[5]*Electron Tube Division #2, Hamamatsu Photonics K.K., 314-5 Shimokanzo, Iwata, Shizuoka 438-0193, Japan*
[6]*Department of Neurosurgery, School of Medicine, Iwate Medical University, 19-1 Uchimaru, Morioka 020-8505, Japan*
[7]*Department of Microbiology, School of Medicine, Iwate Medical University, 19-1 Uchimaru, Morioka 020-8505, Japan*

(Received April 10, 2006; accepted June 25, 2006; published online October 6, 2006)

A microfocus X-ray tube is useful for performing magnification radiography, and its X-ray generator (L9631, Hamamatsu Photonics) consists of a personal computer for controlling the tube voltage and current, and a main unit with a high-voltage circuit and a fixed-anode X-ray tube. The maximum tube voltage, current, and electric power were 110 kV, 800 μA, and 50 W, respectively. The focal-spot size was proportional to the electric power of the tube, and the size was approximately 20 μm with a power of 20 W. Using a 3-mm-thick aluminum filter, the X-ray intensity was 7.75 μGy/s at 1.0 m from the source with a tube voltage of 60 kV and a current of 100 μA. Because the peak photon energy was approximately 38 keV using the filter with a tube voltage of 60 kV, the bremsstrahlung X-rays were absorbed effectively by iodine-based contrast media at an iodine K-edge of 33.2 keV. Enhanced angiography was performed by fourfold magnification imaging with a computed radiography system using iodine-based microspheres 15 μm in diameter. In the angiography of nonliving animals, we observed fine blood vessels of approximately 100 μm with high contrast. [DOI: 10.1143/JJAP.45.8005]

KEYWORDS: high-contrast angiography, magnification digital radiography, microfocus X-ray tube, energy-selective imaging

1. Introduction

To perform high-speed medical radiography, several various flash X-ray generators using cold-cathode tubes have been developed.[1–4] In particular, quasi-monochromatic flash X-ray generators[5–10] have been designed to perform preliminary experiments for producing clean K-series X-rays, and higher-harmonic hard X-rays have been observed in a weakly ionized linear plasma of copper and nickel. However, in monochromatic flash radiography, difficulties in increasing X-ray duration and in performing X-ray computed tomography (CT) have been encountered.

Synchrotrons are capable of producing high-dose-rate monochromatic parallel X-ray beams using silicon crystals, and the beams have been applied to phase-contrast radiography[11,12] and enhanced K-edge angiography.[13,14] In angiography, monochromatic X-rays with photon energies ranging from 33.3 to 35 keV have been employed because the rays are absorbed effectively by iodine-based contrast media with an iodine K-edge of 33.2 keV.

Without using synchrotrons, phase-contrast radiography[15] for edge enhancement can be performed using a microfocus X-ray tube, and the enhancement has been achieved in mammography[16] with a computed radiography (CR) system[17] using a 100-μm-focus tube. Subsequently, we developed a cerium X-ray generator[18,19] to perform enhanced K-edge angiography using cone beams, and succeeded in observing fine blood vessels and coronary arteries with high contrast using cerium Kα-rays of 34.6 keV.

Although the magnification radiography is used to improve the spatial resolution in angiography utilizing a digital imaging system, it is difficult to design a small focus cerium tube for angiography. Therefore, narrow-photon-energy bremsstrahlung X-rays[20–22] with a peak energy of approximately 35 keV from a tungsten tube are used to perform high-contrast angiography.

In this research, we employed a microfocus tungsten tube, and performed enhanced magnification angiography by controlling bremsstrahlung X-ray spectra using an aluminum filter.

2. Principle of Enhanced Magnification Angiography

Figure 1 shows the mass attenuation coefficients of iodine at the selected energies; the coefficient curve is discontinuous at the iodine K-absorption edge of 33.2 keV. The effective bremsstrahlung X-rays for K-edge angiography are shown above the K-edge. Using a 3.0-mm-thick aluminum filter for absorbing soft X-rays, the peak photon energy of the bremsstrahlung rays increases to approximately 38 keV. In angiography, iodine contrast media in blood vessels easily absorb the rays, and soft bremsstrahlung rays are absorbed effectively by objects (muscles). Therefore, blood vessels are observed with high contrast. Subsequently, spatial resolution is improved by fourfold magnification imaging using a microfocus X-ray tube in conjunction with a CR system (Regius 150, Konica Minolta) at a sampling pitch of 87.5 μm.

3. Experimental Methods

The microfocus X-ray generator (L9631, Hamamatsu Photonics) consists of a personal computer and a system unit. The unit includes all the hardware in the X-ray generator, such as, a high-voltage circuit and a fixed anode X-ray tube. Tube voltage, current, and exposure time can be controlled by the computer. The maximum tube voltage, current, and electric power were 110 kV, 800 μA, and 50 W,

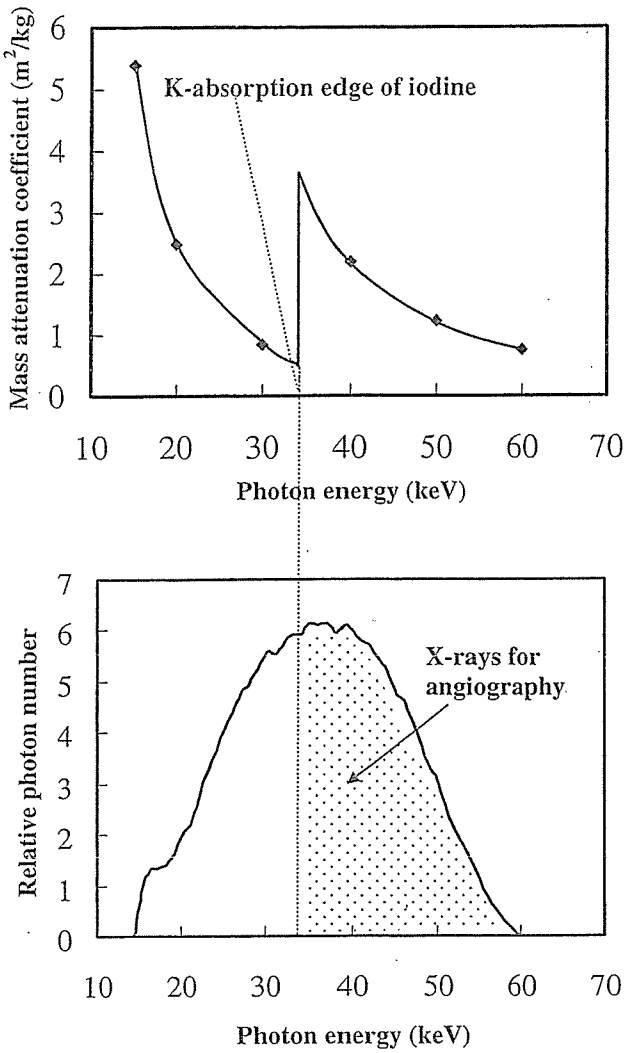

Fig. 1. Mass attenuation coefficients of iodine and bremsstrahlung X-rays for enhanced K-edge angiography.

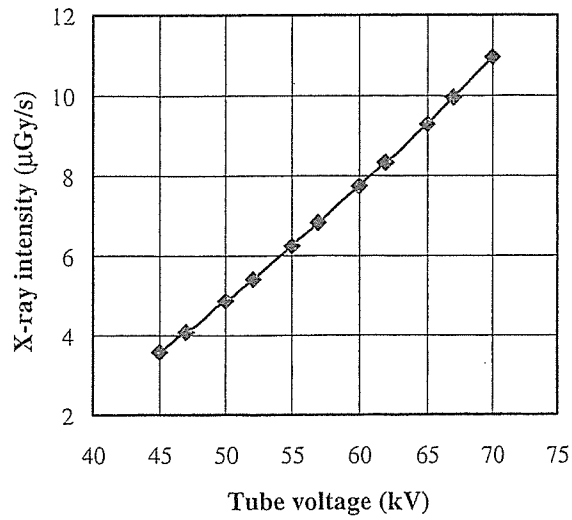

Fig. 2. X-ray intensity (μGy/s) as a function of tube voltage (kV) with tube current of 100 μA.

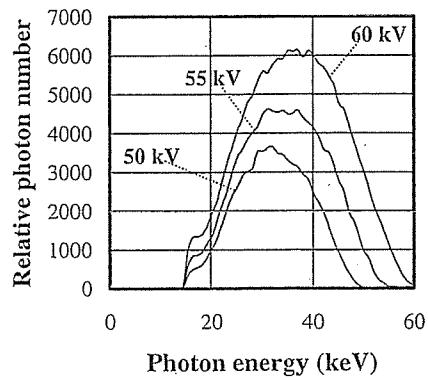

Fig. 3. Bremsstrahlung X-ray spectra measured using cadmium telluride detector with changes in tube voltage.

respectively. The focal-spot size was proportional to the electric power of the tube, and its size was approximately 20 μm in diameter with a power of 20 W. In this experiment, the tube voltage applied ranged from 45 to 70 kV, and the tube current was regulated to within 170 μA. The exposure time is controlled to obtain optimum X-ray intensity for angiography, and narrow-photon-energy bremsstrahlung X-rays are produced using the aluminum filter.

4. Results

4.1 X-ray intensity

X-ray intensity was measured using a Victoreen 660 ionization chamber, with a volume of 400 cm^3, at 1.0 m from the X-ray source using the filter (Fig. 2). At a constant tube current of 100 μA, X-ray intensity increased when tube voltage was increased. At a tube voltage of 60 kV, the X-ray intensity with the filter was 7.75 μGy/s.

4.2 X-ray spectra

To measure X-ray spectra using the filter, we employed a cadmium telluride detector (CDTE2020X, Hamamatsu Photonics) (Fig. 3). When tube voltage was increased, bremsstrahlung X-ray intensity increased, and both maximum photon energy and spectrum peak energy increased.

To perform K-edge angiography, bremsstrahlung X-rays of approximately 35 keV are used; the high-energy bremsstrahlung X-rays decrease image contrast. When this filter was used, because bremsstrahlung X-rays with energies higher than 60 keV were not absorbed easily, the tube voltage for angiography was determined to be 60 kV by considering the filtering effect of radiographic objects.

4.3 Enhanced magnification angiography

The enhanced angiography was performed by fourfold magnification imaging using the CR system and the filter at a tube voltage of 60 kV, and the distance between the X-ray source and the imaging plate was 1.0 m (Fig. 4). First, the spatial resolutions of cohesion and magnification radiographies were realized using a lead test chart at an exposure time of 30 s. In the magnification radiography, 50-μm-thick lines (10 line pairs) were clearly visible (Fig. 5). Figure 6 shows radiograms of tungsten wires in a 25-mm-diameter rod made of poly(methyl methacrylate) (PMMA) at an exposure time of 30 s. Although image contrast decreased slightly with decreasing wire diameter owing to the blurring of the image caused by the sampling pitch of 87.5 μm, a 20-μm-diameter wire could be observed.

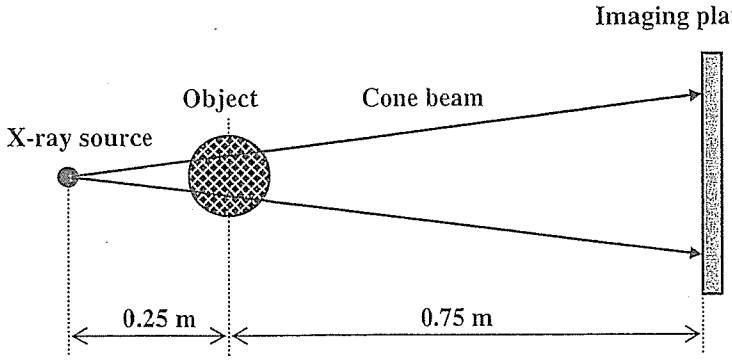

Fig. 4. Fourfold magnification imaging using imaging plate in conjunction with microfocus tube.

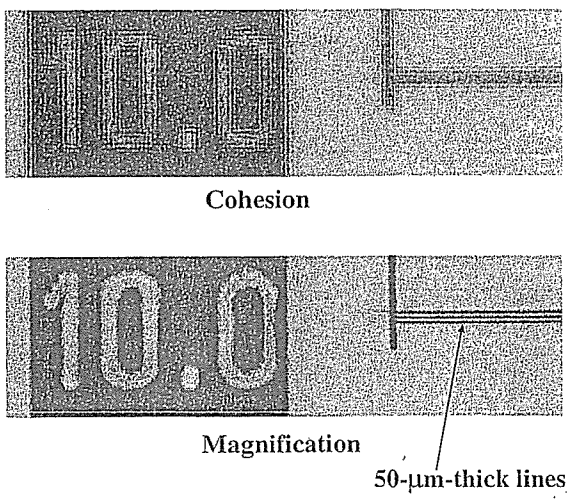

Fig. 5. Radiogram of test chart for measuring spatial resolution.

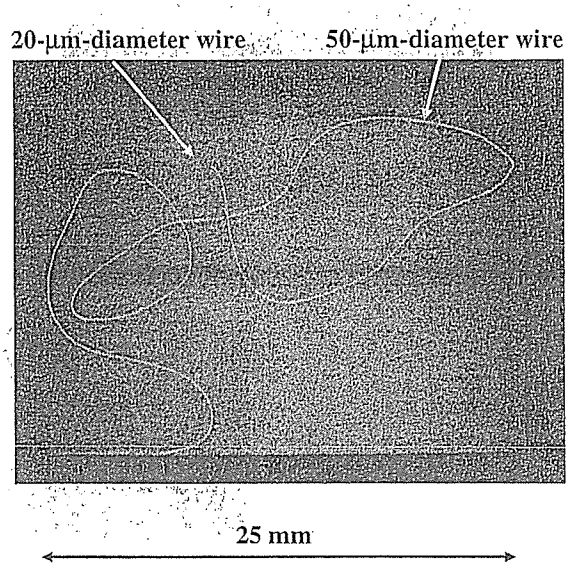

Fig. 6. Radiograms of tungsten wires in PMMA rod.

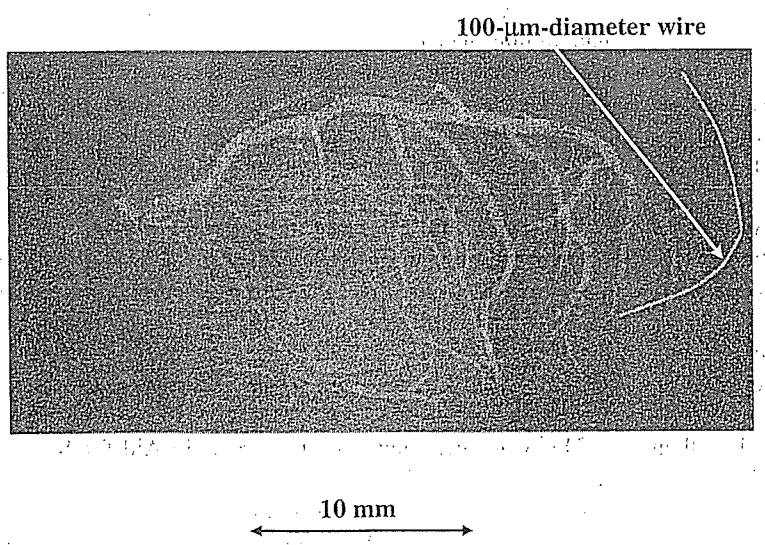

Fig. 7. Angiogram of extracted rabbit heart using iodine microspheres.

Figures 7 and 8 show angiograms of a 19-mm-thick rabbit heart specimen and a 41-mm-thick thigh specimen, respectively. The exposure time was 30 s, and these images were obtained using iodine microspheres of 15 μm diameter. The microspheres are very useful for making the phantoms of nonliving animals used for angiography. The iodine plastic spheres contained 37% iodine by weight, and the coronary arteries and fine blood vessels were visible.

Figure 9 shows angiograms of a dog heart specimen of 65 mm thickness using iodine spheres with an exposure time of 60 s. Although the image contrast decreased slightly with increasing thickness of the PMMA plate facing the X-ray

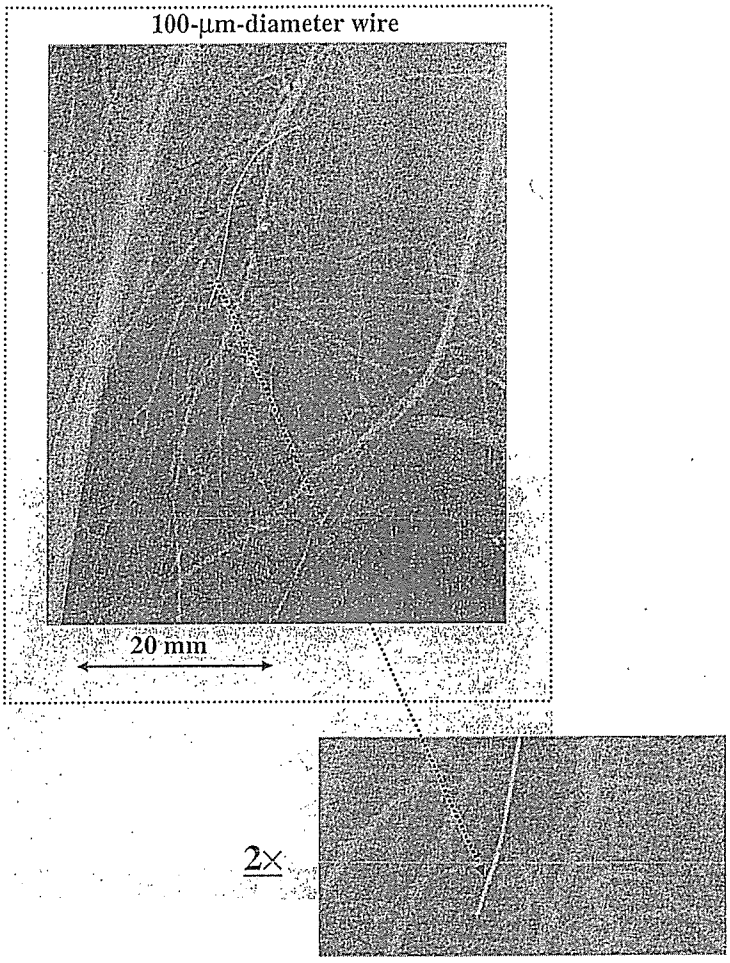

Fig. 8. Angiograms of rabbit thigh.

source, the coronary arteries of approximately 100 μm diameter were observed using a 100-mm-thick plate.

5. Conclusions

We employed a microfocus X-ray generator with a tungsten target tube to perform enhanced magnification angiography using narrow-photon-energy bremsstrahlung X-rays at a peak photon energy of approximately 38 keV, which can be absorbed easily by iodine-based contrast media. Although bremsstrahlung X-ray intensity substantially increased with increasing tube voltage, the optimal tube voltage for increasing image contrast was determined to be 60 kV.

Because the sampling pitch of the CR system is 87.5 μm, we obtained spatial resolutions of approximately 50 μm using fourfold magnification imaging achieved with a 20-μm-focus tube. To observe fine blood vessels of less than 100 μm diameter, the spatial resolution of the CR system should be improved to 43.8 μm (Regius 190, Konica Minolta), and iodine density should be increased.

In this research, we controlled bremsstrahlung X-rays to the optimum spectral distribution for realizing enhanced angiography using iodine-based contrast media. On the other hand, gadolinium-based contrast media with a K-edge energy of 50.2 keV have been employed to perform angiography in MRI, and the gadolinium density used has been increasing. In view of this situation, tungsten Kα rays (58.9 keV) are useful for enhancing K-edge angiography, because the Kα rays are absorbed effectively by gadolinium media. As compared with angiography using iodine media, the absorbed dose can be decreased considerably using gadolinium media.

At a tube voltage of 60 kV and a current of 170 μA, the photon number was approximately 2×10^7 photons/(cm^2·s) at 1.0 m from the source, and photon count rate can be increased easily using a rotating anode microfocus tube developed by Hitachi Medical Corporation. Recently, the maximum electric power of the microfocus X-ray tube has been increasing, and a kilowatt-range tube is realizable. Therefore, real-time magnification radiography will become possible using a flat panel detector with a pixel size of less than 100 μm.

Acknowledgments

This work was supported by Grants-in-Aid for Scientific Research (13470154, 13877114, and 16591222) and Advanced Medical Scientific Research from MECSST, Health and Labor Sciences Research Grants (RAMT-nano-001, RHGTEFB-genome-005 and RHGTEFB-saisei-003), and grants from the Keiryo Research Foundation, Promotion and Mutual Aid Corporation for Private Schools of Japan, Japan Science and Technology Agency (JST), and New Energy and Industrial Technology Development Organization (NEDO, Industrial Technology Research Grant Program in '03).

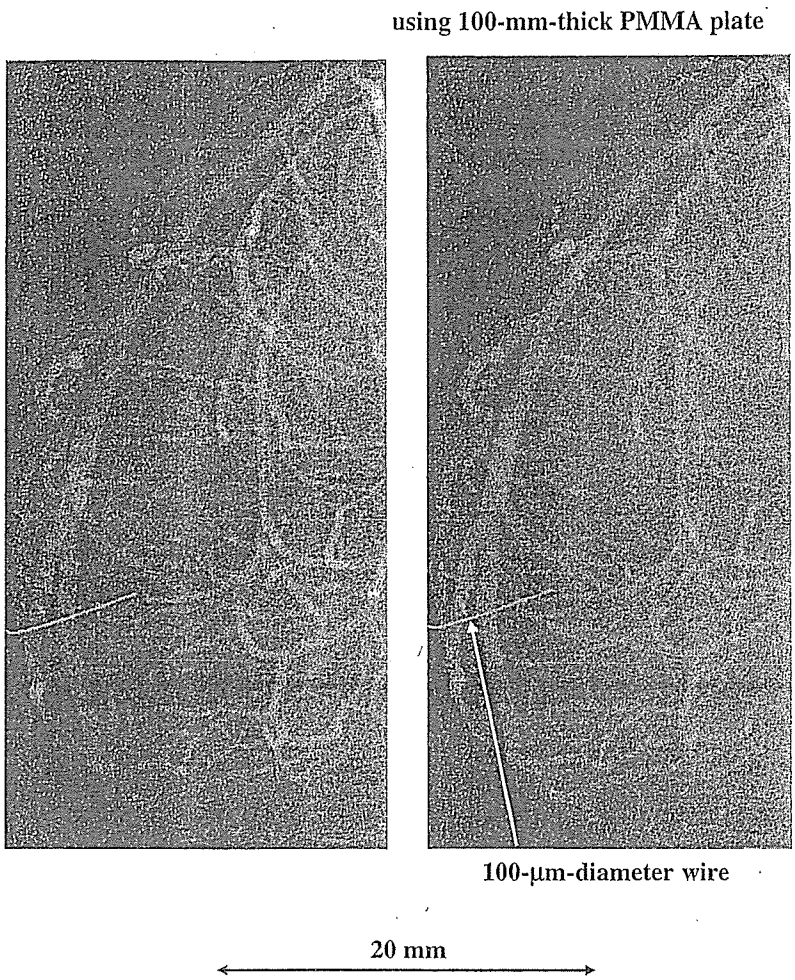

Fig. 9. Angiograms of extracted dog heart.

1) E. Sato, S. Kimura, S. Kawasaki, H. Isobe, K. Takahashi, Y. Tamakawa and T. Yanagisawa: Rev. Sci. Instrum. **61** (1990) 2343.
2) K. Takahashi, E. Sato, M. Sagae, T. Oizumi, Y. Tamakawa and T. Yanagisawa: Jpn. J. Appl. Phys. **33** (1994) 4146.
3) E. Sato, K. Takahashi, M. Sagae, S. Kimura, T. Oizumi, Y. Hayasi, Y. Tamakawa and T. Yanagisawa: Med. Biol. Eng. Comput. **32** (1994) 289.
4) E. Sato, M. Sagae, K. Takahashi, A. Shikoda, T. Oizumi, Y. Hayasi, Y. Tamakawa and T. Yanagisawa: Med. Biol. Eng. Comput. **32** (1994) 295.
5) E. Sato, Y. Hayasi, R. Germer, E. Tanaka, H. Mori, T. Kawai, T. Ichimaru, K. Takayama and H. Ido: Rev. Sci. Instrum. **74** (2003) 5236.
6) E. Sato, Y. Hayasi, R. Germer, E. Tanaka, H. Mori, T. Kawai, T. Ichimaru, S. Sato, K. Takayama and H. Ido: J. Electron Spectrosc. Relat. Phenom. **137–140** (2004) 713.
7) E. Sato, E. Tanaka, H. Mori, T. Kawai, S. Sato and K. Takayama: Opt. Eng. **44** (2005) 049002.
8) E. Sato, M. Sagae, E. Tanaka, Y. Hayasi, R. Germer, H. Mori, T. Kawai, T. Ichimaru, S. Sato, K. Takayama and H. Ido: Jpn. J. Appl. Phys. **43** (2004) 7324.
9) E. Sato, E. Tanaka, H. Mori, T. Kawai, T. Ichimaru, S. Sato, K. Takayama and H. Ido: Med. Phys. **32** (2005) 49.
10) E. Sato, Y. Hayasi, K. Kimura, E. Tanaka, H. Mori, T. Kawai, T. Inoue, A. Ogawa, S. Sato, K. Takayama, J. Onagawa and H. Ido: Jpn. J. Appl. Phys. **44** (2005) 8716.
11) A. Momose, T. Takeda, Y. Itai and K. Hirano: Nat. Med. **2** (1996) 473.
12) M. Ando, A. Maksimenko, H. Sugiyama, W. Pattanasiriwisawa, K. Hyodo and C. Uyama: Jpn. J. Appl. Phys. **41** (2002) L1016.
13) H. Mori, K. Hyodo, E. Tanaka, M. U. Mohammed, A. Yamakawa, Y. Shinozaki, H. Nakazawa, Y. Tanaka, T. Sekka, Y. Iwata, S. Honda, K. Umetani, H. Ueki, T. Yokoyama, K. Tanioka, M. Kubota, H. Hosaka, N. Ishizawa and M. Ando: Radiology **201** (1996) 173.
14) K. Hyodo, M. Ando, Y. Oku, S. Yamamoto, T. Takeda, Y. Itai, S. Ohtsuka, Y. Sugishita and J. Tada: J. Synchrotron Radiat. **5** (1998) 1123.
15) S. W. Wilkins, T. E. Gureyev, D. Gao, A. Pogany and A. W. Stevenson: Nature **384** (1996) 335.
16) A. Ishisaka, H. Ohara and C. Honda: Opt. Rev. **7** (2000) 566.
17) E. Sato, K. Sato and Y. Tamakawa: Annu. Rep. Iwate Med. Univ. School Liberal Arts Sci. **35** (2000) 13.
18) E. Sato, E. Tanaka, H. Mori, T. Kawai, T. Ichimaru, S. Sato, K. Takayama and H. Ido: Med. Phys. **31** (2004) 3017.
19) E. Sato, E. Tanaka, H. Mori, T. Kawai, T. Inoue, A. Ogawa, A. Yamadera, S. Sato, F. Ito, K. Takayama, J. Onagawa and H. Ido: Jpn. J. Appl. Phys. **44** (2005) 8204.
20) A. B. Crummy, C. A. Mistretta, M. G. Ort, F. Kelcz, J. R. Cameron and M. P. Siedband: Radiology **8** (1973) 402.
21) R. A. Kruger, C. A. Mistretta, A. B. Crummy, J. F. Sackett, M. M. Goodsit, S. J. Riederer, T. L. Houk, C. G. Shaw and D. Flemming: Radiology **125** (1977) 234.
22) F. Kelcz and C. A. Mistretta: Med. Phys. **3** (1977) 159.

Tokai J Exp Clin Med., Vol. 31, No. 2, pp. 49-52, 2006

Efficient Preparation of Cationized Gelatin for Gene Transduction

Naoto FUKUYAMA, Tsuyoshi ONUMA[*1], Shio JUJO, Yoshifumi TAMAI[*2], Takahiro SUZUKI[*3], Kazunori MYOJIN[*4], Yasuhiko TABATA[*5], Yoshimi ISHIHARA[*1], Jiro TAKANO[*1] and Hidezo MORI[*6]

*Department of Physiology, [*2] Department of Radiation Oncology,*
*[*3] Department of Ophthalmology, [*4] Department of Radiology, Tokai University School of Science*
*[*1] Department of Chemistry, Tokai University School of Science*
*[*5] Department of Frontier Medical Sciences, Kyoto University*
*[*6] Department of Cardiac Physiology, National Cardiovascular Center*

(Received November 21, 2005; Accepted April 12, 2006)

We previously reported gene therapy using cationized gelatin microspheres of ϕ20-32 μm, prepared from pig skin, as a transducing agent, but although the gelatin offered various advantages, its yield was extremely low (only 0.1%). In this study, we markedly improved the yield of ϕ20-32 μm cationized gelatin microspheres and prepared a newly less than ϕ20 μm cationized gelatin. Conventionally, cationized gelatin is prepared by cationization, particulation by agitation, and cross-linking. The yield is determined by the particulation step, for which we had used a three-necked distillation flask of 500 mL and an agitation speed of 420 rpm. The yield was significantly increased from 0.13 ± 0.02% to 8.80 ± 1.90% by using a smaller flask of 300 mL and an agitation speed of 25000 rpm ($p < 0.01$). We could also prepare cationized gelatin of less than ϕ20 μm, which had not been possible previously. We confirmed that efficient gene introduction into peritoneal macrophages could be achieved with the new cationized gelatin.

Key words: gelatine microsphere, macrophage, yield

INTRODUCTION

Efficient gene transduction methods are necessary for gene therapy [1], and currently available methods can be divided into viral vector techniques and non-viral approaches, such as lipofection or electroporation. Viral vectors such as adenovirus or retrovirus offer high transduction efficiency, but there are questions regarding safety [2]. On the other hand, the efficiency of transduction with non-viral vectors is generally poor [3]. In recent years, nucleofection has been developed for highly efficient gene transduction, but it can be applied to only certain cells, and it causes damage in some cases [4].

We showed that intramuscular injection of FGF-4 gene-gelatin complex induced significantly greater angiogenesis than injection of the bare FGF-4 gene [5]. Furthermore, we showed that adrenomedullin (AM) gene-gelatin complex effectively transduced the AM gene into endothelial progenitor cells (EPCs), and the transduced EPCs had a therapeutic effect in pulmonary hypertension [6]. In those studies, we used cationized gelatin microspheres of ϕ20-32 μm, derived from pig skin. However, the yield of gelatin was only about 0.1%. Cascone *et al.* reported that the preparation of nanoparticulate gelatin required an agitation speed of cationized gelatin and olive oil of more than 10,000 rpm [7], so in this study, we examined whether the use of a higher agitation speed during preparation of the gelatin particles would increase the yield and reduce the particle size in our procedure. We also confirmed the efficacy of the gelatin particles thus obtained for gene transduction.

MATERIALS

Gelatin of pig skin origin (PI 9) was purchased from Nitta Gelatin Corp, Japan. 1-Ethyl-3-(3-dimethylaminopropyl) carbodiimide (EDC), β-alanine, acetone, glycine, hydrochloric acid, ethylenediamine, olive oil, glutaraldehyde solution (GA), potassium dihydrogenphosphate, disodium hydrogenphosphate and sodium hydrogen carbonate were purchased from Wako Pure Chemical Industry, Japan. Liquid nitrogen was purchased from Tomoe Corporation, Japan.

Rat peritoneal macrophages were collected by intraperitoneal injection of thioglycolate culture medium as previously described [8]. DNA encoding GFP with the cytomegalovirus enhancer-chicken β-actin hybrid promoter was constructed [5].

METHODS

Conventional preparation of gelatin microspheres involves three steps: (1) cationized gelatin production, (2) microsphere production and (3) cross-linking of cationized gelatin microspheres. In order to increase the yield of cationized gelatin microspheres, we aimed to improve the second step, i.e., microsphere production.

Cationized gelatin production

PI 9 (10 g) was completely dissolved in 0.1 M phosphate buffer (PBS, 450 mL) containing potassium dihydrogenphosphate and disodium hydrogenphosphate. Ethylenediamine (31.1 mL) and hydrochloric acid were added, and the pH was adjusted to 5.0. EDC (5.35 g) was added to this solution, which was made up to 500 mL with PBS and left for 18 hours. The solution was

Naoto FUKUYAMA or Hidezo MORI, Department of Physiology, Tokai University, Bohseidai, Isehara, Kanagawa 259-1193, Japan Tel: +81-463-931-121 Fax: +81-463-936-684 E-mail: fukuyama@is.icc.u-tokai.ac.jp

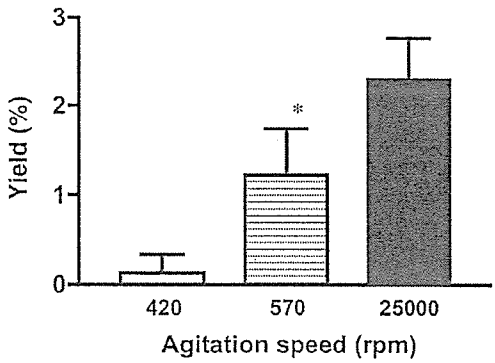

Fig. 1 Yield of ϕ20-32 μm cationized gelatin using a 500 mL three-necked distillation flask.
The open bar shows the control (420 rpm) group, horizontal lined bar, the 570 rpm group and closed bar, the 25,000 rpm group. Data are presented as mean ± SEM. The yield in the 570 rpm group was significantly higher than that in the control group (*p <0.001 vs 420 rpm).

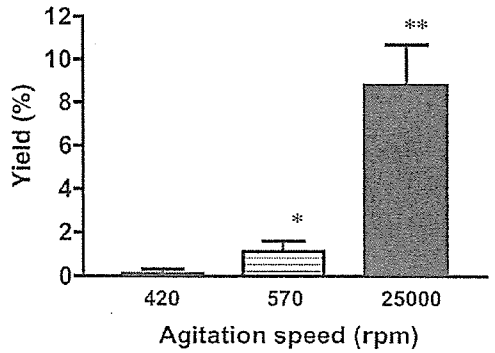

Fig. 2 Yield of ϕ20-32 μm cationized gelatin using a 300 mL three-necked distillation flask.
The open bar shows the 420 rpm group, horizontal lined bar, the 570 rpm group and closed bar, the 25,000 rpm group. Data are presented as mean ± SEM. The yield in the 570 rpm group was significantly higher than that in the 420 rpm group (*p < 0.001 vs 420 rpm). The yield in the 25,000 rpm group was significantly higher than that in the other groups (**p <0.0001 vs other groups).

then dialyzed for 2 days with 16 changes of water. After the dialysis, this solution was freeze-dried for 4 to 7 days to afford cationized gelatin. The conversion rate of carboxyl groups to amino groups was measured by the TNBS method to characterize the product [13].

Microsphere production

In the conventional procedure, cationized gelatin aqueous solution and olive oil were placed in a three-necked distillation flask of 500 mL at 40°C, and centrifuged at 420 rpm for 10 minutes. This solution was stirred for 30 minutes at 0°C. Acetone was added, and the mixture was centrifuged. After centrifugation, the oil layer was removed, and acetone was added. This solution was centrifuged again, homogenized and sieved with ϕ20 μm, ϕ32 μm and ϕ90 μm sieves (Test sieves, #JIS Z 8801, Tokyo Screen Co., Ltd., Japan). The microspheres was dried in a refrigerator overnight, and the yield of each fraction was determined.

In this experiment, we examined the effect of increasing the agitation speed to 570 rpm and 25000 rpm, and the effect of using a smaller three-necked distillation flask (300 mL) to obtain smoother mixing.

Cross-linking of cationized gelatin microspheres

Acetone and hydrochloric acid (7:3) were added to cationized gelatin microspheres, the crosslinking agent GA was added, and the reaction was allowed to proceed for 24 hours. After the reaction, centrifugation was performed and the supernatant was removed. Glycine solution (100 mM) was added to remove GA for one hour. After centrifugation, the supernatant was removed and cross-linked microspheres were cooled with liquid nitrogen, freeze-dried, and weighed.

Gene introduction with the newly developed cationized gelatin microspheres

Gene gelatin complex was prepared by mixing 2 mg of cationized gelatin and 50 μg/100 μl gene (GFP or luciferase). The complex was incubated with rat peritoneal macrophages for 14 days. Effective gene introduction was demonstrated by cellular expression of GFP or luciferase.

RESULTS

Effect of agitation conditions on yield of cationized gelatin

In the conventional method (500 mL/420 rpm), the yield of the ϕ20-32 μm cationized gelatin was 0.13 ± 0.02%, but when the agitation speed was increased to 570 rpm, the yield rose to 1.22 ± 0.52% (*p < 0.001 vs 420 rpm). The yield was further increased to 2.30 ± 0.47% by increasing the agitation speed to 25000 rpm from 570 rpm, but this further increase was not statistically significant (p=0.136)(Fig. 1). Next we used a smaller (300 mL) three-necked distillation flask with agitation at 420 rpm, 570 rpm and 25,000 rpm. When the agitation speed was increased to 570 rpm, the yield rose to 1.12 ± 0.49% from 0.11 ± 0.01% (*p <0.001 vs 420 rpm). The yield was markedly increased to 8.80 ± 1.90% by increasing the agitation speed to 25,000 rpm from 570 rpm (**p <0.0001 vs 420 or 570 rpm) (Fig. 2).

The yields of different-sized microsphere fractions are summarized in Table 1. The use of the highest agitation speed and the smaller flask allowed us to obtain cationized gelatin microspheres of less than ϕ20 μm, which we had not been able to prepare with the conventional method, in addition to increasing the total yield of the cationized gelatin microspheres.

Gene introduction with the new cationized gelatin

We examined the efficiency of the new, smaller-sized cationized microspheres for gene introduction into rat peritoneal macrophages. As shown in Figure 3A, after coincubation of the macrophages and GFP

Table 1 Yields of different-sized cationized gelatines (%).

Flask size (mL) / Agitation speed (rpm)	$>\phi$20 μm	ϕ20-32 μm	ϕ32-90 μm	ϕ90 μm $>$
500/420	0	0.13±0.02	15.1±3.21	14.0±5.30
500/570	0	1.22±0.52*	13.2±3.52	14.1±6.13
500/25000	0	2.30±0.47	17.2±4.10	7.23±1.60
300/420	0	0.11±0.01	19.1±5.32	17.4±7.12
300/570	0	1.12±0.49**	22.1±7.62	11.3±2.52
300/25000	2.12±0.21	8.80±1.90***	32.2±11.0	9.10±2.10

Data are presented as mean ± SEM. *p $<$0.001 vs 500/420, **p $<$0.001 vs 300/420
***p $<$0.0001 vs 300/420 or 300/570

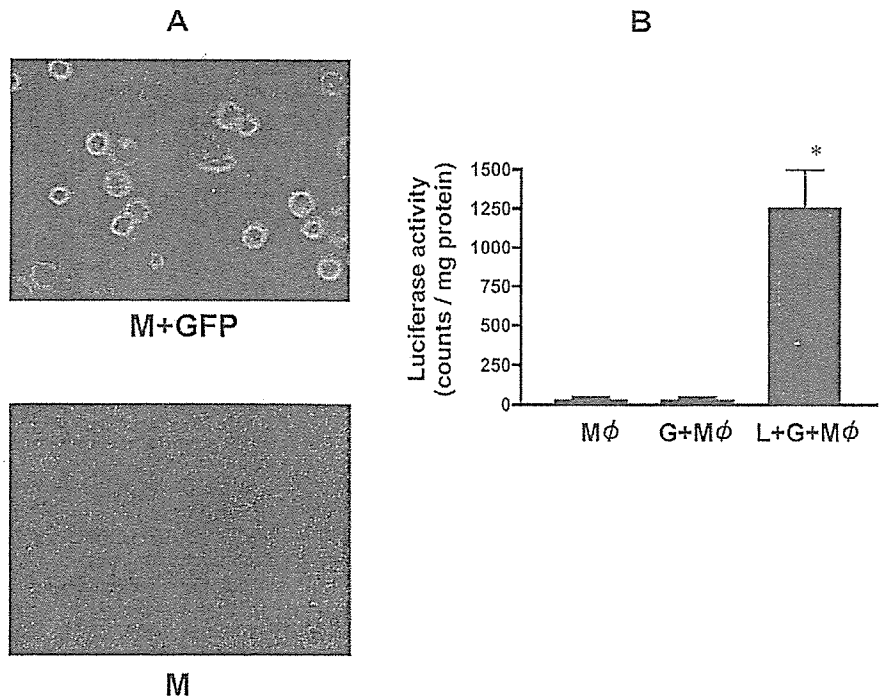

Fig. 3 Gene introduction into rat peritoneal macrophages with cationized gelatin.
A. Upper column: Peritoneal macrophages were coincubated with GFP gene-cationized gelatin complex (M + GFP) for 14 days. GFP was expressed in the cytoplasm of the macrophages. Lower column: Peritoneal macrophages were coincubated with cationized gelatin complex (M) for 14 days. GFP was not expressed in the macrophages.
B. Luciferase activity. Peritoneal macrophages were coincubated with luciferase gene-cationized gelatin complex (L + G + Mϕ, closed bar) or with cationized gelatin (G + Mϕ, horizontal lined bar) or with no additive (Mϕ, open bar) for 14 days. Data are presented as mean ± SEM. The luciferase activity of L+G+Mϕ was significantly higher than that of Mϕ or G+Mϕ (*p $<$0.01).

gene-cationized gelatin complex, the cells expressed GFP. Coincubation of the macrophages and cationized gelatin alone did not result in expression of GFP. As shown in Figure 3B, after coincubation of the macrophages and luciferase gene-cationized gelatin complex, the cells expressed luciferase activity of 1251 ± 257 (counts/mg protein) on day 14, while the activity in the control group, in which macrophages were cultured alone, was only 5 ± 2 (counts/mg protein) (*p $<$0.01). The luciferase activity was 8 ± 2 (count/mg protein) in the macrophage + cationized gelatin group.

DISCUSSION

In this study, we showed that the yield of cationized gelatin microspheres of ϕ20-32 μm increased with increasing agitation speed and with the use of a smaller three-necked flask for the agitation of cationized gelatin with olive oil. In addition, cationized gelatin microspheres smaller than ϕ20 μm could be prepared for the first time with the highest agitation speed and the smaller flask.

In the conventional method, 30% of cationized

gelatin finally formed microspheres, but almost all were larger than ϕ32 μm [9]. Gene introduction with cationized gelatin microspheres involves cellular phagocytic activity, which is inefficient for particles as large as ϕ30 μm [6]. By using a speed as high as 25,000 rpm and a smaller flask (300 mL), we were able to increase the yield of cationized gelatin microspheres of ϕ20-32 μm to 8.80%. Furthermore, we could manufacture cationized gelatin microspheres smaller than ϕ20 μm, which could not be obtained by the conventional method, in a yield of 2.12%.

Gedanken *et al.* succeeded in the production of nanoparticles from various chemicals by using ultrasonic irradiation [10]. However, when we used an ultrasonic homogenizer for agitating cationized gelatin and olive oil, the yield decreased to 1.30% .

We previously showed that our gelatin microsphere-gene complexes were introduced into cells by phagocytosis. Since the efficiency of cellular phagocytotic activity is greater for smaller particles, the development of smaller-sized cationized gelatin microspheres is expected to increase the efficiency of gene introduction via phagocytosis. Further, Kaul *et al.* showed that gene introduction into fibroblasts, which exhibit endocytosis but not phagocytosis, was possible by using nanoparticles of polyethylene glycol [11]. Therefore, if our method can be extended to obtain cationized gelatin microspheres in the nano size range, the variety of cells to which they would be applicable may be considerably extended. It is still the case that a gene introduction method with adequate safety and efficiency for clinical application is not yet available [12]. The ingredient, gelatin, used in this study is already in clinical use, and is considered to be safe. Cationized gelatin microspheres cannot be used to introduce genes into all types of cells, and the efficiency of gene introduction is lower than that of viral vectors. However, the use of cationized gelatin microspheres to introduce a gene into endothelial progenitor cells did have an apparent and prolonged therapeutic effect [5, 6]. The smaller cationized gelatin microspheres developed in this study may provide increased efficiency of gene introduction into various cells.

In conclusion, we have improved the preparation of cationized gelatin microspheres for gene transduction, obtaining a greater yield, as well as smaller microspheres, which may have clinical potential.

ACKNOWLEDGEMENT

This work was supported by grants from Tokai University School of Medicine Research Aid in 2004 and 2005, the research and study program of Tokai University Educational System General Research Organization and Kanagawa Nanbyou foundation in 2004, as well as a Grant-in-Aid for Scientific Research in 2003 (No. 15659285) and 2005 (No. 17659375) from the Ministry of Education, Science and Culture, Japan and Health and Labour Sciences Research Grants for Research on Human Genome, Tissue Engineering Food Biotechnology in 2003 (H15-saisei-003). Health and Labour Sciences Research Grants for comprehensive Research on Cardiovascular Diseases in 2004 (H16-jyunkannki(seishuu)-009).

REFERENCES

1) Pfeifer A, Verma IM.: Gene therapy: promises and problems. Annu Rev Genomics Hum Genet 2: 177-211, 2001.
2) Kay MA, Glorioso JC, Naldini L.: Viral vectors for gene therapy: the art of turning infectious agents into vehicles of therapeutics. Nat Med 7: 33-40, 2001.
3) Ferber D.: Gene therapy. Safer and virus-free? Science 294: 1638-42, 2001.
4) Schakowski F, Buttgereit P, Mazur M, Marten A, Schottker B, Gorschluter M, Schmidt-Wolf IG.: Novel non-viral method for transfection of primary leukemia cells and cell lines. Genet Vaccines Ther 2: 1, 2004.
5) Kasahara H, Tanaka E, Fukuyama N, Sato E, Sakamoto H, Tabata Y, Ando K, Iseki H, Shinozaki Y, Kimura K, Kuwabara E, Koide S, Nakazawa H, Mori H.: Biodegradable gelatin hydrogel potentiates the angiogenic effect of fibroblast growth factor 4 plasmid in rabbit hindlimb ischemia. J Am Coll Cardiol 41: 1056-62, 2003.
6) Nagaya N, Kangawa K, Kanda M, Uematsu M, Horio T, Fukuyama N, Hino J, Harada-Shiba M, Okumura H, Tabata Y, Mochizuki N, Chiba Y, Nishioka K, Miyatake K, Asahara T, Hara H, Mori H.: Hybrid cell-gene therapy for pulmonary hypertension based on phagocytosing action of endothelial progenitor cells. Circulation 108: 889-95, 2003.
7) Cascone MG, Lazzeri L, Carmignani C, Zhu Z.: Gelatin nanoparticles produced by a simple W/O emulsion as delivery system for methotrexate. J Mater Sci Mater Med 13: 523-6, 2002.
8) Kittlick PD, Engelmann D.: The glycosaminoglycans in cultures of stimulated rat peritoneal macrophages. 2. Gel chromatographic studies and the behaviour of heparan sulfate. Exp Toxicol Pathol 45: 87-92, 1993.
9) Fukunaka Y, Iwanaga K, Morimoto K, Kakemi M, Tabata Y.: Controlled release of plasmid DNA from cationized gelatin hydrogels based on hydrogel degradation. J Control Release 80: 333-43, 2002.
10) Gedanken A.: Using sonochemistry for the fabrication of nanomaterials. Ultrason Sonochem 11: 47-55, 2004.
11) Kaul G, Amiji M.: Cellular interactions and in vitro DNA transfection studies with poly(ethylene glycol)-modified gelatin nanoparticles. J Pharm Sci 94: 184-198, 2004.
12) Tomanin R, Scarpa M.: Why do we need new gene therapy viral vectors? Characteristics, limitations and future perspectives of viral vector transduction. Curr Gene Ther 4: 357-72, 2004.
13) Rabinovich-Guilatt L, Couvreur P, Lambert G, Goldstein D, Benita S, Dubernet C.: Extensive surface studies help to analyse zeta potential data: the case of cationic emulsions. Chem Phys Lipids 131: 1-13, 2004.